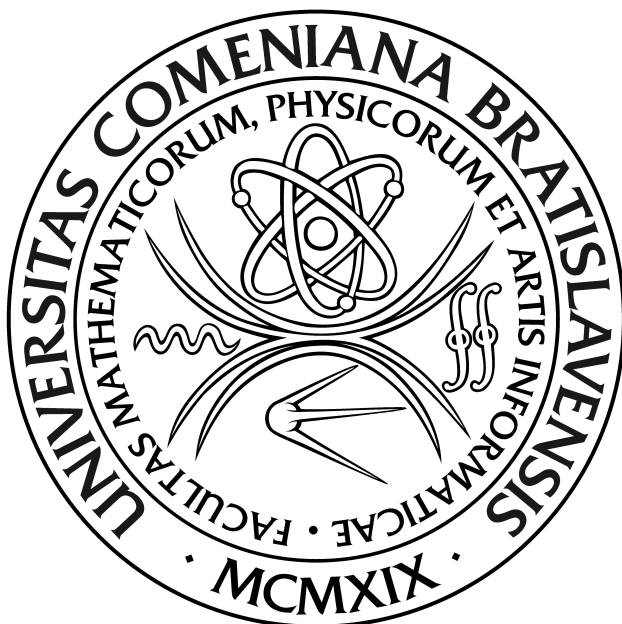


Comenius University
Faculty of Mathematics, Physics and Informatics

BACHELOR THESIS



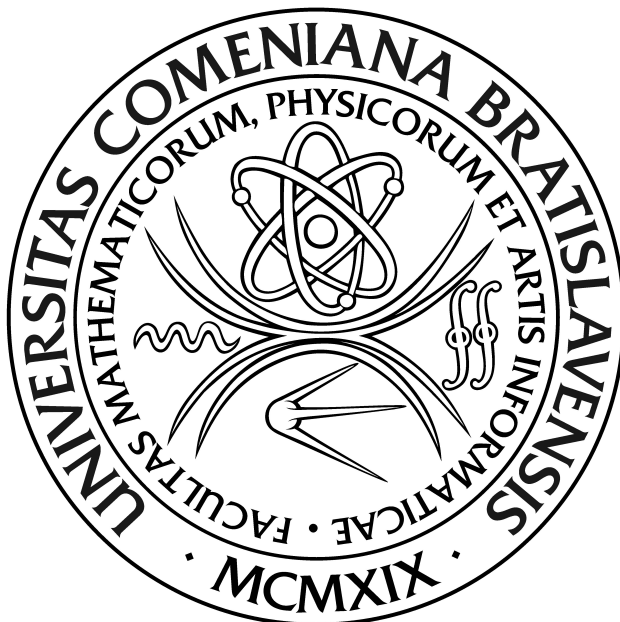
Jakub Bahyl

Measurement of Quantum Turbulence in Superfluid Helium Using Second Sound Attenuation

Bratislava, 2016

Comenius University
Faculty of Mathematics, Physics and Informatics

BACHELOR THESIS



Jakub Bahyl

Measurement of Quantum Turbulence in Superfluid Helium Using Second Sound Attenuation

Department of Low Temperature Physics, Charles University in Prague

Study programme: Physics

Study programme number: 1160

Supervisor of the bachelor thesis: RNDr. David Schmoranzer, Ph.D.

Consultant of the bachelor thesis: Dr. Martin James Jackson, Ph.D.

Bratislava, 2016



THESIS ASSIGNMENT

Name and Surname:

Jakub Bahyl

Study programme:

Physics (Single degree study, bachelor I. deg., full time form)

Field of Study:

Physics

Type of Thesis:

Bachelor's thesis

Language of Thesis:

English

Secondary language:

Slovak

Title: Measurement of Quantum Turbulence in Superfluid 4He Using Second Sound Attenuation

Aim: During the work on this Thesis, the student will become familiar with the theoretical foundations of the description of quantum fluids and superfluidity. The student will learn about several experimental methods used for characterization of the flows of superfluid helium, such as second sound attenuation, which differs significantly from any techniques used in classical fluids. Given the focus of the Thesis, classical hydrodynamics will be used as a stepping-stone to help in the understanding of quantum fluids. On the practical side, the student will learn to design and run complex cryogenic experiments. This work will cover a wide range of skills, starting with the understanding of safety procedures for handling cryoliquids, of specific measures needed for operation of experiments with liquid helium at temperatures between 1.2 K and 4.2 K, and including work with sensitive electronic detectors such as quartz tuning forks, as well as a fundamental understanding of modern automated data acquisition and processing.

Literature:

- [1] L.D. Landau, E.M. Lifshitz, Fluid Mechanics, Pergamon Books, 1987
- [2] L. Skrbek a kol., Fyzika nízkých teplot, Matfyzpress, 2011
- [3] D.R. Tilley, J. Tilley, Superfluidity and Superconductivity, Adam Hilger, 1986
- [4] R.J. Donnelly: Quantized vortices in helium II, Cambridge University Press, 2005
- [5] E. Varga, S. Babuin, L. Skrbek, Second-sound studies of coflow and counterflow of superfluid He-4 in channels, Phys. Fluids 27(6), 065101 (2015)
- [6] Vinen, W. F. Mutual friction in a heat current in liquid helium II. II. Experiments on transient effects. Proceedings of the Royal Society of London A: Mathematical, Physical and Engineering Sciences. 240, 1220 (1957).
- [7] R. Blaauwgeers, M. Blažková, M. Človečko, V.B. Eltsov, R. de Graaf, J. Hosio, M. Krusius, D. Schmoranzer, W. Schoepe, L. Skrbek, P. Skyba, R.E. Solntsev, D.E. Zmeev: Quartz Tuning Fork: Thermometer, Pressure- and Viscometer for Helium Liquids, J. Low Temp. Phys. 146, 537-562 (2007)
- [8] S.L. Ahlstrom, D.I. Bradley, M. Človečko, S.N. Fisher, A.M. Guénault, E.A. Guise, R.P. Haley, O. Kolosov, P.V.E. McClintock, G.R. Pickett, M. Poole, V. Tsepelin, and A.J. Woods, Phys. Rev. B 89, 014515 (2014).

Annotation:

The main focus of this Thesis will be study of oscillatory flows of superfluid helium at low temperatures. Specifically, we will characterize the transition to



Comenius University in Bratislava
Faculty of Mathematics, Physics and Informatics

turbulence in a flow due to an oscillating tuning fork, combining, for the first time, two different methods simultaneously. The first technique will rely on standard drag force measurements performed using the tuning fork, while at the same time, second sound attenuation will be used to determine the density of quantized vortices in the flow. The principal question we will tackle is whether classical turbulence and quantum turbulence form at the same time in the given flow, or whether they can be observed separately in a subset of the parameter space defined by the tuning fork velocity and an effective Reynolds number. This work is directly related to ongoing research at the Laboratory of Superfluidity operated by the Faculty of Mathematics and Physics of the Charles University in Prague.

Supervisor: David Schmoranzer

Rektorát, dekanát: FMFI.Dek - Faculty Administration

Assigned: 29.10.2015

Approved: 29.10.2015

prof. RNDr. Jozef Masarik, DrSc.

Guarantor of Study Programme

.....
Student

.....
Supervisor

Acknowledgments

My special thanks go to my supervisor, David Schmoranzer, who gave me a lot of experiences, knowledge and much more of his time, without which I definitely could not write this Thesis. Together with consultant Martin Jackson, they guided me during the whole experiment and helped me to understand all the important aspects included in this work. Moreover, I am thankful to Ladislav Skrbek and Patrik Švančara for giving me such a great opportunity to find out how astounding the experimental physics can be and to work with Superfluidity group within Charles University in Prague.

In the end, I would like to hugely thank my friends and family for all their „*Good luck*” and „*Keep going*” motivational quotes and other sort of supports, which I deeply appreciated.

I declare that I carried out this bachelor thesis independently, and only with the cited sources, literature and other professional sources.

In date

Signature of the author:

Názov práce

Meranie kvantovej turbulencie v supratekutom héliu pomocou útlmu druhého zvuku

Autor

Jakub Bahyl

Školiteľ bakalárskej práce

RNDr. David Schmoranzer, Ph.D.

Abstrakt

V tejto práci prezentujeme meranie kvantovej turbulencie generovanej oscilujúcim 6.5 kHz kremenným oscilátorom, ponoreným v supratekutom ${}^4\text{He}$ pri viacerých teplotách pod kritickou $T_\lambda = 2.17\text{ K}$. Pozorovaná nelineárna odporová sila pôsobiaca na oscilátor je kvalitativne spôsobená prítomnosťou klasickej turbulencie a kvantovaných vírov. Odporové sily a množstvo vytvorených kvantovaných vírov (hustota vírov čiar L) sú nepriamo určené z útlmu druhého zvuku a mechanicko-elektrických vlastností oscilátora. Výsledky, ktoré prezentujeme, kvantitatívne charakterizujú tvorbu klasickej aj kvantovej turbulencie. Ako prví ukazujeme, že obidve turbulencie vedia vzniknúť samostatne a nezávisle. Tento fakt je prezentovaný, v prvom priblížení, pomocou *prúdového fázového diagramu*, v ktorom pre danú teplotu vieme predpokladať, kedy a ktorá turbulencia vzniká.

Kľúčové slová

fyzika nízkych teplôt • supratekutosť ${}^4\text{He}$ • kvantová turbulencia • hydrodynamika

Title

Measurement of quantum turbulence in superfluid helium using second sound attenuation

Author

Jakub Bahyl

Supervisor

RNDr. David Schmoranzer, Ph.D.

Abstract

In this work we present measurements of quantum turbulence generated by a 6.5 kHz oscillating quartz tuning fork submerged in superfluid ${}^4\text{He}$ at various temperatures below $T_\lambda = 2.17\text{ K}$. The observed non-linear drag acting on the tuning fork is qualitatively described by a presence of classical turbulence and quantized vortices. Drag forces and the amount of produced quantized vortices (the vortex line density L) are determined indirectly by the attenuation of second sound and by the measurement of mechanical and electrical properties of the tuning fork. We present results which characterize quantitatively the formation of classical and quantum turbulence. For the first time, we show that both turbulences can arise separately. This is presented, in first approximation, via a *flow phase diagram*, where for a given temperature, one can predict when each type of turbulence forms.

Keywords

low temperature physics • superfluidity • quantum turbulence • hydrodynamics

Contents

Introduction	2
1 Theoretical Background	3
Superfluidity	3
1.1 Helium-II as a Bose-Einstein Condensate	4
1.2 Two-Fluid Model	5
1.3 Second Sound	7
Quantum Effects	8
1.4 Quantized Vortices	9
1.5 Quantum Turbulence	11
1.6 Second Sound Attenuation	12
Fluid Dynamics	14
1.7 From Laminar to Turbulent Flow	15
1.8 Drag Forces Acting on Submerged Objects	16
1.9 Oscillatory Motion in a Viscous Fluid	17
1.10 Oscillations in Superfluid He-II	18
2 Experimental Setup	20
2.1 Quantum Turbulence Generator	20
2.2 Second Sound Source and Detector	21
2.3 The Apparatus	22
2.4 Measurement Methods	24
3 Results	26
3.1 Measurement of Vortex Line Density	27
3.2 Drag Force Measurements	31
3.3 Correlation of Results	34
3.4 Discussion	38
4 Conclusions	40
Bibliography	42

Introduction

The discovery of helium's liquid state kick-started modern experimental low temperature physics. In 1908, the Dutch physicist Heike Kamerlingh Onnes reached the liquid state of helium at 4.2K for the very first time. With this, the last known gas was finally liquefied. Later, in 1913, Onnes was awarded the Nobel Prize for "*his investigations on the properties of matter at low temperatures which led to the production of liquid helium*".

Later studies proved the existence of a new liquid state of ${}^4\text{He}$ - the superfluid phase, known as He-II. The transition (known as the λ transition) occurs at $T_\lambda \approx 2.17\text{ K}$. The full phase diagram is shown in **Figure 1**.

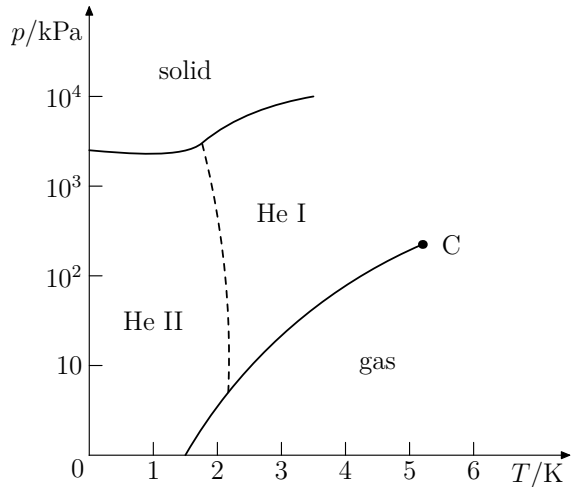


Figure 1: The pressure-temperature phase diagram of ${}^4\text{He}$. At atmospheric pressure and a temperature of 4.2 K, ${}^4\text{He}$ condenses into a liquid, known as He-I. As we cool further, helium becomes a superfluid, denoted as He-II on the phase diagram, below $T_\lambda \approx 2.17\text{ K}$. From the phase diagram, one will note that even at absolute zero, helium does not become solid. This is due to the weak van der Waals interaction between helium atoms and the fact that the zero-point oscillations of the helium atoms are so strong, that no solid is stable unless pressurized to above 2.5 MPa.

While the properties and behaviour of He-I are similar to classical viscous fluids, He-II exhibits significantly different properties. For example, the thermal conductivity is amongst the highest of any known material. Later, in 1937 Pyotr Kapitsa[1] conducted a few experiments on superfluid flow through narrow capillaries. He observed that He-II was able to flow with negligible viscosity. This research was also recognized by a Nobel prize in 1978.

The phenomenological description of these effects, the *two-fluid model*, was provided by Tisza and Landau. Together with the theory of Bose-Einstein condensation and quantum mechanics, these theories provide a basic understanding of superfluidity.

Moreover, superfluidity allows for the existence of vortices with discretely quantized circulation. These vortices are composed of circulating superfluid around a narrow core and can tangle to produce quantum turbulence (QT). QT is measurable using specific experimental methods, some of which will be described later in this work.

1. Theoretical Background

The theoretical part of this Thesis is composed of three chapters:

1. The first serves as a brief introduction to the topic of superfluidity using Bose-Einstein statistical physics and basic hydrodynamics.
2. The second chapter focuses on macroscopic quantum effects of superfluids, and introduces the concept of quantized vortices using quantum mechanics.
3. The last theoretical chapter deals with fluid dynamics; particularly the drag coefficients for various structures in fluid flows. We will also introduce the Reynolds number for oscillating objects immersed in both classical and quantum fluids.

All of the ideas discussed in this chapter can be found in standard textbooks [7], [4] except for the derivation of the vortex line density at the end of second part, where the original papers of Feynman, Vinen and Hall are required [10], [12], [13].

Superfluidity

Among all chemical substances, helium is special and unique at low temperatures. Under normal conditions (room temperature and atmospheric pressure), helium gas behaves as an ideal gas and the most common isotope is ^4He , formed by 2 protons, 2 neutrons and 2 electrons.¹ Due to the composition of the ^4He atom, the resulting nuclear spin is equal to zero. Therefore, ^4He is a boson and obeys Bose-Einstein quantum statistics. This will be discussed in more detail in **Section 1.1**.

When cooled below $T_\lambda = 2.17\text{ K}$, ^4He undergoes a second-order phase transition to the superfluid state and quantum effects become much more significant. Since the quantum mechanical wave function for bosons is symmetric, two arbitrary atoms can occupy the same quantum state. The Pauli exclusion principle does not apply to bosons, so the global state of He-II at low temperatures can be described as a considerable amount of particles sitting in the energy ground state.

We can therefore describe the whole He-II fluid as two inter-penetrating fluids, one composed of ground-state particles (and described by the macroscopic wave function) - the condensate or superfluid component, and a second classical-like fluid composed of thermally excited atoms - the normal fluid component. In the following sections, this *two-fluid model* will be used to describe the rotational motion of the superfluid and consequently, the existence of quantum turbulence.

¹There is another stable isotope of Helium, ^3He , which has one less neutron in the nucleus. In this Thesis, we will only focus on the isotope ^4He .

1.1 Helium-II as a Bose-Einstein Condensate

The total spin of ${}^4\text{He}$ is zero, so gaseous helium may be classified as a Bose gas. Additionally, if we assume no interactions between the particles, we may use the *ideal Bose gas* model. This of course cannot provide a perfect description of helium's behaviour (due to its weak interactions), but it will suffice. The thermodynamic limit of the ideal Bose model provides an intuitive insight to helium's special properties, such as superfluidity.

Quantum Statistics

We choose to work with a scaled inverted temperature $\beta \equiv 1/kT$ and chemical potential μ , denoting the number of particles sitting in the state $|n\rangle$ as N_n and corresponding energy as ε_n .² A mathematical description of such a quantum system can be done through Bose-Einstein statistics. In this statistical model of a grand canonical ensemble, a given state can be independently occupied by an arbitrary number of particles. Hence, we write the grand canonical potential Φ as:

$$\Phi(T, V, \mu) = -\beta^{-1} \ln \left[\prod_n \sum_{N_n=0}^{\infty} e^{-\beta N_n (\varepsilon_n - \mu)} \right] = \beta^{-1} \sum_n \ln(1 - e^{-\beta(\varepsilon_n - \mu)}), \quad (1.1)$$

where we assumed $\mu < 0$ for the purpose of convergence. If we think of each particle as a de Broglie wave with wavelength $\lambda \sim \hbar/p \sim \hbar/(\varepsilon m)^{1/2}$, one can calculate the mean value of the total number of particles sitting in all thermal levels by replacing the sum with an integral over all possible wave numbers:

$$\langle N \rangle = -\frac{\partial \Phi}{\partial \mu} = \sum_n \frac{1}{e^{\beta(\varepsilon_n - \mu)} - 1} \approx \frac{V}{(2\pi)^3} \int d^3k \frac{1}{e^{\beta(\varepsilon_k - \mu)} - 1} + N_0, \quad (1.2)$$

where the term N_0 , representing the number of ground state particles, has been added as a correction. By integrating (1.2), this correction appears to be relevant only when the temperature of system reach the critical value (as shown in [2]):

$$T_c = \frac{2\pi\hbar^2}{mk} \left(\frac{N}{V\zeta(3/2)} \right)^{2/3}, \quad (1.3)$$

where $\zeta(3/2) \approx 2.612$ is the value of Riemann zeta-function. If we substitute to (1.3) the values of N, V and m , specific for ${}^4\text{He}$, we would predict that the critical temperature should be $T_c \approx 3.15$ K, which is not far from the observed superfluid transition at $T_\lambda = 2.17$ K.

As temperature $T < T_c$ decreases, more and more particles, a macroscopic number N_0 , will occupy a single quantum state and form the so-called *Bose-Einstein condensate*.

²The entire set of energies are positive $\{\varepsilon_n\} > 0$ except for the ground state, for which we choose $\varepsilon_0 = 0$.

Heat Capacity

More evidence proving the close relation between superfluidity of ^4He and Bose-Einstein condensation is the behaviour of the heat capacity around the critical temperature.

From figure **Figure 1.1** one can see that derivatives of both heat capacities (predicted by BEC and observed using ^4He) are not continuous around critical temperatures (T_c, T_λ). Such discontinuities are often one of the characteristic properties of a phase transition in an infinite system. Since heat capacity is partial derivative of energy $C_V = \partial E / \partial T|_V$, the second derivative would be discontinuous in this case, so therefore we classify the transition to the superfluid state as a 2nd order phase transition. Note that the shape of heat capacity plot as a function of temperature is reminiscent of the Greek letter λ . This is the reason we call the superfluid transition *the λ -transition* and denote the transition temperature as T_λ .

Transition to a superfluid phase can be also found in ^3He (a fermion) at much lower temperatures $\sim 1\text{ mK}$. Although fermions cannot condense, they can form *Cooper pairs*, in analogy with superconductors. These bound states are effectively bosons and therefore can undergo condensation.

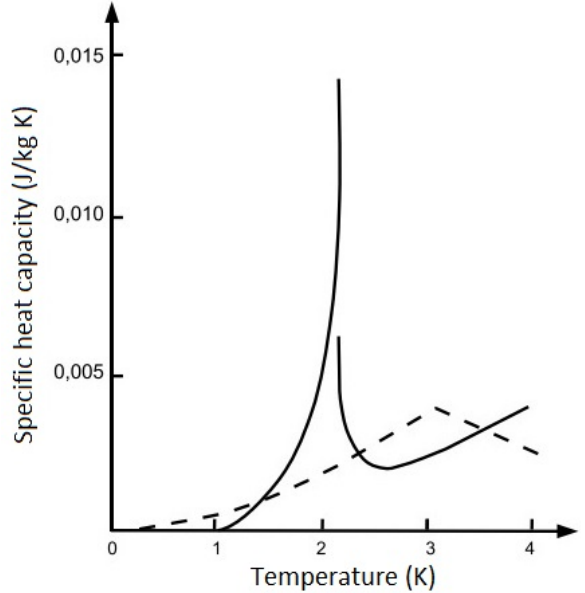


Figure 1.1: Heat capacity of an ideal BEC (dashed line) and that measured for ^4He (full line) as a function of temperature.

1.2 Two-Fluid Model

Observations of superfluid helium led Tisza[3] and Landau[4] to postulate their own theories describing the phenomena. Both assumed that macroscopically the whole fluid is composed of two inter-penetrating fluids. We recognize them as a *normal* and pure *superfluid* component with respective densities ρ_n, ρ_s and velocity fields $\mathbf{v}_n, \mathbf{v}_s$. At low relative velocities, the behaviour of both fluids can be considered as independent. However, the two components can interact through so-called *mutual friction*, which will be discussed later in this work.

The total density ρ can be written as the sum of the normal ρ_n and superfluid ρ_s components:

$$\rho = \rho_n + \rho_s .$$

The densities ρ_n, ρ_s vary with temperature due to decreasing mean value of statistical thermal excitations with reduced temperature. In 1947, L.D. Landau proposed[5] the full

microscopic theory of He-II from which the temperature dependence of the superfluid density was found to be given by $\rho_s \propto -T^3$ below 0.6 K and $\rho_s \propto -T^{1/2}e^{-\varepsilon/T}$ at higher temperatures.

The first experiment proving Landau's theory was done by Andronikashvili[6]. He submerged a stack of tightly packed discs forming a torsional oscillator in He-II to determine the fractional densities from the periods of oscillations. The corresponding fractional densities are plotted in **Figure 1.2**.

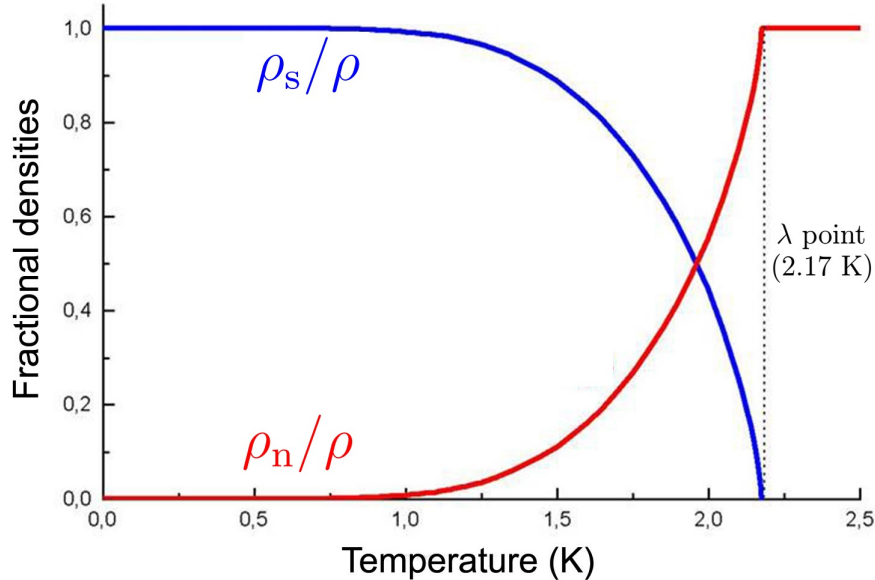


Figure 1.2: Temperature dependence of fractional densities of the normal (red) and superfluid (blue) components. The total density ρ varies only weakly with temperature.

Hydrodynamic Equations of the Two-Fluid Model

Because we are working with more general forms of fluid motion, a generalised dynamic equation has to be derived, too. Due to incompressibility of the fluid and entropy conservation (assuming non-dissipative processes), the continuity equations must hold:

$$\frac{\partial \rho}{\partial t} = -\nabla \cdot (\rho_n \mathbf{v}_n + \rho_s \mathbf{v}_s), \quad (1.4)$$

$$\frac{\partial(\rho s)}{\partial t} = -\nabla \cdot (s\rho \mathbf{v}_n). \quad (1.5)$$

We are only missing the equations of motion for each of the two fluid components. They should have a form similar to the Navier-Stokes equation but with a few differences. We expect a mutual friction term, connecting both equations of motion, and a missing viscous term within the equation for the superfluid component.

The full derivation of the two-fluid equations of motion is fairly complicated and can be found in standard low temperature physics textbooks (such as [7]).

The most general form of the motion equations for both, the normal and superfluid component, respectively are:

$$\rho_n \left[\frac{\partial \mathbf{v}_n}{\partial t} + (\mathbf{v}_n \cdot \nabla) \mathbf{v}_n \right] = - \frac{\rho_n}{\rho} \nabla P - \rho_s S \nabla T - \frac{\rho_n \rho_s}{2\rho} \nabla (\mathbf{v}_n - \mathbf{v}_s)^2 + \mathbf{F}_{ns} + \eta_n \nabla^2 \mathbf{v}_n , \quad (1.6)$$

$$\rho_s \left[\frac{\partial \mathbf{v}_s}{\partial t} + (\mathbf{v}_s \cdot \nabla) \mathbf{v}_s \right] = - \frac{\rho_s}{\rho} \nabla P + \rho_s S \nabla T + \frac{\rho_n \rho_s}{2\rho} \nabla (\mathbf{v}_n - \mathbf{v}_s)^2 - \mathbf{F}_{ns} , \quad (1.7)$$

where P is the applied pressure and η_n denotes the viscosity of the normal component. The terms containing ∇T and $\nabla(\mathbf{v}_n - \mathbf{v}_s)^2$ can be viewed as additional pressure effects.

Considering the simplest case, no thermal flow ($\nabla T = 0$), counterflow ($\mathbf{v}_n - \mathbf{v}_s = \mathbf{0}$) nor mutual friction ($\mathbf{F}_{ns} = \mathbf{0}$) is present, we have a classical hydrodynamic system. In fact, (1.6) would reduce to the Navier-Stokes equation for a classical fluid and (1.7) to the Euler equation for an ideal fluid without viscosity. Consequently, the two-fluid model seems to be applicable as a macroscopic approach to the overall behaviour of superfluid ${}^4\text{He}$.

1.3 Second Sound

The two-fluid model has an important consequence for wave behaviour of He-II. If we combine the continuity equations (1.4), (1.5) and the equations of motion (1.6), (1.7), we obtain (the particular method can be found in [8]) two wave equations. The first one describes a classical pressure-density wave with a corresponding velocity u_1 :

$$\frac{\partial^2 \rho}{\partial t^2} = u_1^2 \nabla^2 \rho \quad u_1 = \left(\frac{\partial P}{\partial \rho} \right)_S^{1/2} . \quad (1.8)$$

The second wave equation describes *second sound*, an entropy-temperature wave with a velocity u_2 , given by

$$\frac{\partial^2 s}{\partial t^2} = u_2^2 \nabla^2 s \quad u_2 = \left(\frac{\rho_s}{\rho_n} \frac{T s^2}{C_p} \right)^{1/2} , \quad (1.9)$$

where C_p is the specific heat. The first equation (1.8) represents an ordinary sound, when both fluids oscillate identically ($\mathbf{v}_n = \mathbf{v}_s$). On the contrary, the second wave equation (1.9) describes a new wave process, specific to ${}^4\text{He}$, when the components oscillate in anti-phase ($\rho_s \mathbf{v}_n = -\rho_n \mathbf{v}_s$). Consequently, the total density ρ is constant at every point, but the relative densities ρ_n, ρ_s oscillate. This, consequently, can be viewed as the oscillation of temperature

In our work, the only significant changes in second sound velocity occur as we approach the lambda transition from below. At temperatures above 2.0 K, the second sound velocity starts to drop rapidly and tends towards zero at the lambda point.

Quantum Effects

As we may have seen in the previous chapter, the macroscopic behaviour of He-II is well determined by quantum statistical physics and Landau's two-fluid model. Since the superfluid component flows without dissipation (carrying no entropy), and is (indirectly) related to the atoms in the quantum mechanical ground state, an analogy with electrons orbiting the atomic nucleus can be constructed. This analogy led London to suggest a *macroscopic wave function* $\Psi(\mathbf{r}, t)$ to describe the superfluid component.

Properties of $\Psi(\mathbf{r}, t)$

The wave function $\Psi(\mathbf{r}, t)$ is in general complex and its quadratic norm describes the average number of atoms in the condensate per unit volume: $|\Psi|^2 = \Psi^* \Psi = \rho_s / m_4$, where m_4 is the mass of one ${}^4\text{He}$ atom. The simplest form of $\Psi(\mathbf{r}, t)$ is given as:

$$\Psi(\mathbf{r}, t) = \sqrt{\frac{\rho_s}{m_4}} e^{i\phi(\mathbf{r}, t)}, \quad (1.10)$$

where the phase $\phi(\mathbf{r}, t)$ is an unknown scalar function of spatial coordinates and time. If the whole system is described by a single wave function, the statistical properties are the same and the phases are correlated for all superfluid atoms. We can find out more about the velocity field \mathbf{v}_s by applying the momentum operator $\hat{\mathbf{p}} = \frac{\hbar}{i} \nabla$ on the wave function $\Psi(\mathbf{r}, t)$:

$$\mathbf{v}_s = \frac{\hat{\mathbf{p}}|\Psi\rangle}{m_4|\Psi\rangle} = \frac{\hbar}{i} \frac{\nabla e^{i\phi(\mathbf{r}, t)}}{m_4 e^{i\phi(\mathbf{r}, t)}} = \frac{\hbar}{m_4} \nabla \phi(\mathbf{r}, t). \quad (1.11)$$

According to (1.11), the velocity field \mathbf{v}_s is proportional to the gradient of the scalar field $\phi(\mathbf{r}, t)$, which means the superfluid flow is *potential*³. Moreover, due to the vector calculus identity $\nabla \times (\nabla \phi(\mathbf{r})) = 0$, it turns out that the velocity field \mathbf{v}_s is rotationless. To be more precise, all vorticity vectors equal zero in a simply connected region: $\omega_{\mathbf{v}_s} \equiv \nabla \times \mathbf{v}_s = \mathbf{0}$. The obvious conclusion is that there are no superfluid vortices.

However, this is contrary to observation. One particular experiment, made by Osborne[9], proved the zero vorticity theorem wrong and will be discussed in more detail later in this chapter. The main consequence is that under some circumstances, the condition of space simplicity in He-II might be violated by "holes" in superfluid space. This hole effect directly leads to quantized properties such as *quantized circulation*.

³One can find an equivalent situation in celestial mechanics or electrostatics, where the gravitational and electric potentials can be defined.

1.4 Quantized Vortices

Now we will look at the concept of circulation in more detail. Mathematically, the circulation is a path integral of velocity field along some contour, let call it \mathcal{C} . Generally, \mathcal{C} is an arbitrary closed curve in 3D space with corresponding infinitesimal tangent vectors $d\ell$. Denoting circulation as Γ , we can do the calculation using superfluid velocity field \mathbf{v}_s from (1.11):

$$\Gamma = \oint_{\mathcal{C}} \mathbf{v}_s \cdot d\ell = \frac{\hbar}{m_4} \oint_{\mathcal{C}} \nabla \phi \cdot d\ell. \quad (1.12)$$

From this integral one can get many results, depending on the space connectivity enclosed by loop \mathcal{C} . In the case of no singularities (singly connected region, $\Psi(\mathbf{r}, t) \neq 0$), the calculation is trivial and yields zero⁴. If singularities are present (multiply connected region), there have to be certain places, where $\Psi = 0$. However, the wave function $\Psi \propto \exp\{i\phi(\mathbf{r}, t)\}$ must be defined uniquely everywhere in space. Hence the phase ϕ can change along the loop either by zero or any multiple of 2π . Using the residue theorem from complex calculus we can immediately show that the circulation is quantized:

$$\Gamma = \frac{\hbar}{m_4} \oint_{\mathcal{C}} \nabla \phi \cdot d\ell = \frac{\hbar}{m_4} (\phi_{2\pi} - \phi_0) = \frac{\hbar}{m_4} 2\pi n \equiv n\kappa, \quad (1.13)$$

where κ is called the *circulation quantum*: $\kappa \approx 10^{-7} \text{ m}^2 \cdot \text{s}^{-1}$.

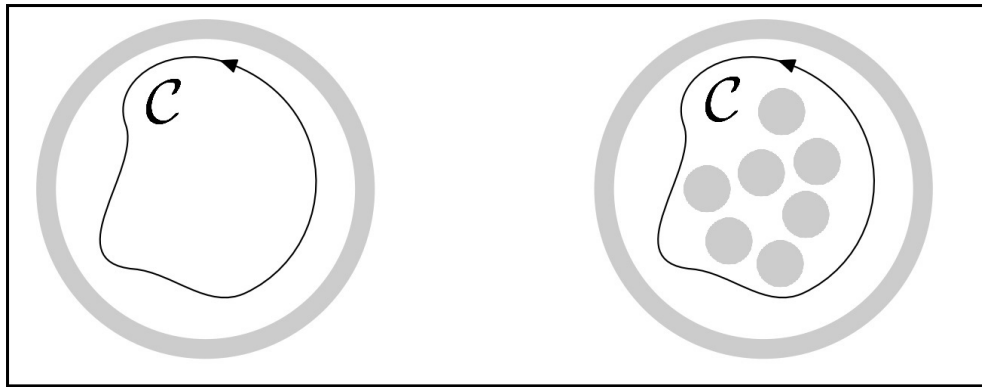


Figure 1.3: Sketch of singly connected region on the left and region containing singularities on the right, enclosed by loop \mathcal{C} . We refer such singularities to the places, where identically $\Psi = 0$. In superfluid He-II, the multiple connected region correspond to the *holes* in superfluid space - the places, where only the normal component is present.

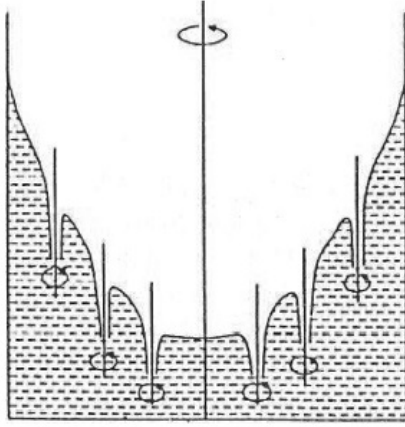
⁴No singularities mean a simple-connectivity of space, so every contour \mathcal{C} may be tightened in a limit to single point. Using Stokes' theorem

$$\Gamma_0 = \oint_{\mathcal{C}_0} \mathbf{v}_s \cdot d\ell = \iint_{S_{\mathcal{C}_0}} (\nabla \times \mathbf{v}_s) \cdot d\mathbf{S} = 0,$$

where we used the fact that $\nabla \times \mathbf{v}_s = \mathbf{0}$.

Experiment Proving the Existence of Quantized Vortices in He-II

In 1950, D.V. Osborne prepared an experiment [9], where a cylindrical container filled with He-II rotates around its principal axis. Since the superfluid component cannot rotate in the classical way, only the normal fluid should take the shape of a parabola. Classical mechanics predicts that the meniscus depth should be flatter as the density of liquid decreases. Surprisingly, Osborne did not observe any depth drop, even when the relative density of normal component was relatively small.



A convincing explanation of this phenomenon was proposed by Richard Feynman[10] predicting the existence of tiny superfluid vortices of discretely quantized circulation. Such vortices ordered in an array within the bulk fluid can mimic macroscopic rotation. Quantitatively, if the angular velocity of the rotating container is Ω , then the classical vorticity is $\omega = \nabla \times \mathbf{v} = 2\Omega$ and the total circulation is - in the case of He-II - composed of circulation quanta κ . From this we can define the *vortex line density* L as the number of quantized vortices intersecting a unit area, or in other words, the total length of all vortices per unit volume:

Figure 1.4: A sketch of rotating container filled with He-II.

$$L = \frac{2\Omega}{\kappa}. \quad (1.14)$$

Basic Properties of a Single Quantized Vortex

From the cylindrical symmetry we can find the velocity field near the vortex core:

$$\oint_C \mathbf{v}_s \cdot d\ell \stackrel{!}{=} n\kappa \quad \longrightarrow \quad \mathbf{v}_s = \frac{\hbar}{m_4 r} n \mathbf{e}_\theta, \quad (1.15)$$

where \mathbf{e}_θ is an unit vector perpendicular to the position vector \mathbf{r} . Near the vortex center, the velocity cannot be arbitrarily big. The highest value is given by the *Landau critical velocity*⁵ which is about $v_L \approx 58 \text{ ms}^{-1}$ at zero pressure. Thus, using (1.15) we can estimate the radius of the core $a_0 = \hbar/m_4 v_L = 0.27 \text{ nm} \approx 3 \text{ \AA}$. A better estimate of a_0 by experiments shows that it is actually about 1 \AA .

We can also calculate the total energy per unit length of a single quantized vortex. This is obtainable by summing up the kinetic energy of the whole circulating superfluid component:

$$\varepsilon_n = \int_a^b \frac{1}{2} \rho_s v_s^2 2\pi r dr = \frac{\pi \hbar^2 \rho_s}{m_4^2} n^2 \int_a^b \frac{dr}{r} = \frac{\pi \hbar^2 \rho_s \ln(b/a)}{m_4^2} n^2 \equiv \varepsilon_0 n^2, \quad (1.16)$$

⁵It is known[11] that exceeding the Landau critical velocity produces thermal excitations.

where ε_0 is the energy per unit length of a singly quantized vortex and b is some characteristic length such as container length or the distance between two vortices. Here we can see that due to $E_{\text{vortex}} \sim n^2$, it is energetically favourable to have singly quantized vortices.

1.5 Quantum Turbulence

Generally, quantized vortex lines do not need to be homogeneously distributed and fully polarized. In situations when these properties are considerably complex, the flow of the superfluid component is strongly chaotic. This randomisation of quantized vortices is known as *quantum turbulence*.

The two-fluid nature of superfluid ^4He definitely provides a more general form of motion of quantum fluids. Consequently, the understanding of such a remarkable physical system as quantum turbulence (QT), may turn to a deeper understanding of turbulence in classical fluids, which is, to this day, far from complete.

Mutual Friction

Each vortex line is composed of the superfluid component rotating around a core of normal fluid. Hence, quantized vortices can interact with both components. In 1957, Vinen and Hall conducted several remarkable experiments[12] to observe this interaction. They measured how the presence of vortices affects the propagation of second sound waves and found out that vortex lines attenuate the second sound signal the same way friction does in the case of a linear mechanical oscillator. By this we mean that the damping is of the form $\sim \exp(-\alpha z)$, where α is the attenuation coefficient and z is the chosen direction of the propagating wave. The attenuation effect was actually expected as the vortices and second sound both represent the relative motion of the two fluid components. Furthermore, the attenuation was found to be stronger when the rotational frequency Ω was increased or when the orientation of the propagating second sound wave was set to be more perpendicular to the vortices.

Combining all the observed properties together, Vinen and Hall laid the foundations[13] for the derivation of the following formula for the mutual friction force:

$$\mathbf{F}_{\text{sn}} = B \frac{\rho_n \rho_s}{\rho} \hat{\boldsymbol{\Omega}} \times [\boldsymbol{\Omega} \times (\mathbf{v}_n - \mathbf{v}_s)] + B' \frac{\rho_n \rho_s}{\rho} [\boldsymbol{\Omega} \times (\mathbf{v}_n - \mathbf{v}_s)]. \quad (1.17)$$

In (1.17), the $\boldsymbol{\Omega}$ stands for the angular velocity of the rotating cryostat, $\hat{\boldsymbol{\Omega}}$ for its normalised vector, $(\mathbf{v}_n - \mathbf{v}_s)$ for the velocity vector of second sound, B and B' are (temperature-dependent) constants. The indices s, n in \mathbf{F}_{sn} represent the case where the superfluid component acts on the normal component. As we might expect, mutual friction is antisymmetric with respect to the indices ($\mathbf{F}_{ns} = -\mathbf{F}_{sn}$).

Now, let us replace the Ω vector with \mathbf{L} from (1.26). Denoting θ as the angle between the vortex line density vector \mathbf{L} and second sound velocity vector $\mathbf{v}_{\text{ns}} = \mathbf{v}_n - \mathbf{v}_s$, and taking only the dissipative term of (1.17) we obtain:

$$\mathbf{F}_{\text{sn}} = -B \frac{\rho_n \rho_s}{2\rho} \kappa L \mathbf{v}_{\text{ns}} \sin^2 \theta.$$

This simplification allows us to calculate an exact expression for the damping factor α of second sound. This formula contains the vortex line density L . Therefore, by measuring the damping factor α in an experiment, we can calculate L . This well-established technique is called the second sound attenuation.

1.6 Second Sound Attenuation

Now we have enough information to derive the attenuation factor of the second sound wave. Let us choose the \mathbf{z} -axis as the second sound wave's direction of propagation. Using (1.5) and equations of motion (1.6), (1.7), the corresponding wave equation takes the form [8]:

$$\frac{\partial^2 \mathbf{v}_{\text{ns}}}{\partial z^2} - \frac{B\kappa L}{2u_2^2} \sin^2 \theta \frac{\partial \mathbf{v}_{\text{ns}}}{\partial t} - \frac{1}{u_2^2} \frac{\partial^2 \mathbf{v}_{\text{ns}}}{\partial t^2} = 0. \quad (1.18)$$

Similar wave equations can be derived by considering for example a damped oscillator or electromagnetic waves in conducting medium. Inspired by Vinen and Hall observations, we seek the solution in the form of an exponentially damped wave:

$$\mathbf{v}_{\text{ns}} = v_0 e^{i(\omega t - kz)} e^{-\alpha z} \mathbf{e}_z, \quad (1.19)$$

where $e^{-\alpha z}$ is the damping factor and $v_0 e^{i(\omega t - kz)} \mathbf{e}_z$ is a counterflow velocity wave propagating in the \mathbf{z} -direction with amplitude v_0 , angular velocity ω and wave vector k . Substituting this result back into (1.18) we obtain the following for the attenuation coefficient:

$$\alpha = \frac{B\kappa L}{4u_2} \sin^2 \theta. \quad (1.20)$$

Of course, the distribution of vortex lines could be generally chaotic and unpredictable, and not only oriented at an angle θ . In a homogeneous and isotropic distribution, we choose rather to work with the mean value of $\sin^2 \theta$ for all directions in 3D space, so the new attenuation constant α^* takes the form:

$$\alpha^* = \frac{B\kappa L}{4c_2} \langle \sin^2 \theta \rangle = \frac{B\kappa L}{6c_2}. \quad (1.21)$$

As we can see, randomly distributed vortex lines attenuates 2/3-times less when compared with the perpendicular interaction with polarized vortices.

Viscous Damping and Resonance Curve

Mutual friction is not the only dissipative effect. While any amount of normal component is still present, classical viscous damping acts even if no quantum turbulence is created. To account for this, the full attenuation should be composed of two constants:

$$\alpha = \alpha_0 + \alpha^*, \quad (1.22)$$

where α_0 is the aforementioned viscous attenuation. Thus when the second sound signal is generated in a finite system, we measure the signal's characteristic resonance curve by changing the frequency. the resonance width Δf of this resonator is related with α , α_0 via:

$$\alpha_0 = \frac{\pi \Delta f_0}{u_2} \quad \alpha = \frac{\pi \Delta f}{u_2}, \quad (1.23)$$

where Δf_0 is the resonance width when no vortex lines are present. Taking out L from (1.21) and using (1.22), (1.23) we get:

$$L = \frac{6c_2}{B\kappa} \alpha^* = \frac{6\pi}{B\kappa} (\Delta f - \Delta f_0). \quad (1.24)$$

The parameters B , Δf_0 and Δf are measurable variables. However, there is a more practical way to measure certain quantities and then calculate L .

Second sound devices usually work on the basis of measuring a voltage across a biased resistive thermometer or across a capacitor made from a semi-permeable membrane placed in a second sound resonator. When on resonance, emitted second sound waves are reflecting back and forth, resulting in a standing wave formed in the resonator. The receiver observes a wave with an amplitude A_0 (when there are no vortices) and a decreased amplitude A , when a number of vortex lines are present. The ratio of these amplitudes can be derived by summing up all the reflected waves and takes the form[14]:

$$\frac{A_0}{A} = \frac{\Delta f}{\Delta f_0}. \quad (1.25)$$

Finally, connecting the results of (1.24) and (1.25) we obtain

$$L = \frac{6\pi \Delta f_0}{B\kappa} \left(\frac{A_0}{A} - 1 \right), \quad (1.26)$$

which allows us to determine the vortex line density by directly measurable parameters.

Fluid Dynamics

Continuum equations cover processes occurring over a wide range of length scales, starting from quantized vortices (10^{-10} m) to galactic motion (10^{20} m). Under certain circumstances, the continuum flow may exhibit irregular, turbulent behaviour (**Figure 1.5**, **Figure 1.6** [15]).

Vortices were observed and painted by Leonardo da Vinci and since then, many theories have been developed but a general theory of turbulence remains elusive. In previous chapters, we introduced the basic properties of superfluid helium, which are governed by quantum mechanical effects. Since all quantized vortices are essentially identical, a description of quantum turbulence *should be* relatively simpler and could lead to the development of a mathematical prototype of turbulence in general.



Figure 1.5: Photograph of laminar flow past a cylinder.

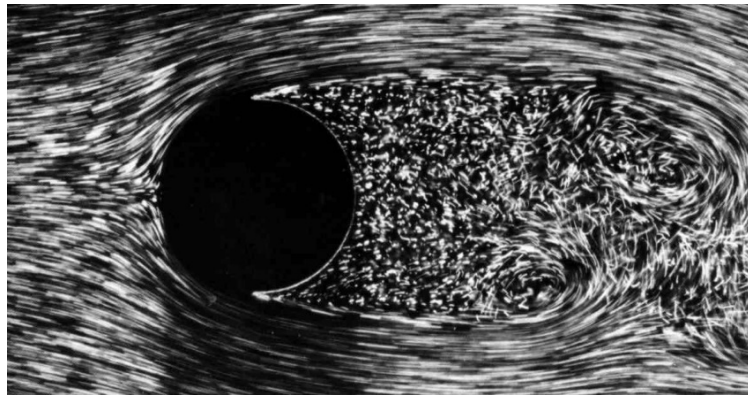


Figure 1.6: Photograph of turbulent flow past a cylinder.

In the following sections, we will present a mathematical description of viscous fluids and their dynamics, focusing on the transition from laminar to turbulent flow and defining the dimensionless *Reynolds number* (Re) and the drag coefficient C_D . Finally, analogical hydrodynamic equations and properties will be defined for He-II as well.

1.7 From Laminar to Turbulent Flow

We define a flow as *laminar* when the velocity field is steady in time and can be characterized by a set of non-intersecting streamlines. Turbulent flow displays chaotic dynamics, it contains vortices of various sizes and circulations and is therefore much harder to characterise than laminar flows. In fact, no exact definition exists.

Let us consider a classical Newtonian viscous fluid. Using the model of continuum physics one arrives[4] at the conservation of the mass, entropy and momentum (Navier-Stokes) equation, which completely determine the density, entropy and velocity fields $\mathbf{v}(\mathbf{r}, t)$ of the fluid at any point in time or space:

$$\frac{\partial \rho}{\partial t} = -\nabla \cdot (\rho \mathbf{v}), \quad (1.27)$$

$$\frac{\partial(\rho s)}{\partial t} = -\nabla \cdot (\rho s \mathbf{v}), \quad (1.28)$$

$$\rho \left[\frac{\partial \mathbf{v}}{\partial t} + (\mathbf{v} \cdot \nabla) \mathbf{v} \right] = -\nabla P + \eta \nabla^2 \mathbf{v} + \rho \mathbf{f}, \quad (1.29)$$

where the last equation is valid only for incompressible fluids. In this case, the continuity equation can be reduced to $\nabla \cdot \mathbf{v} = 0$. Here ρ denotes the fluid density, η the dynamic viscosity and \mathbf{f} sums up all external forces per unit mass. In addition, if we consider the flow as isotropic ($s = \text{const}$), the entire fluid's motion is given by the reduced continuity equation and the Navier-Stokes equation (1.29).

Principle of Dynamical Similarity and Reynolds Number

In many cases, it is useful to transform the stationary ($\partial \mathbf{v} / \partial t = \mathbf{0}$) Navier-Stokes equation (1.29) into a form containing dimensionless parameters. This can be done with the typical (mean) value of the flow velocity v_0 and with the length scale L at which the velocity changes most significantly. All magnitudes appearing in (1.29) are scaled as:

$$\mathbf{v}' \equiv \frac{\mathbf{v}}{v_0} \quad \Bigg| \quad \mathbf{r}' \equiv \frac{\mathbf{r}}{L} \quad \Bigg| \quad \nabla' \equiv L \nabla \quad \Bigg| \quad P' \equiv \frac{P}{P_0} = \frac{P}{\rho v_0^2}.$$

After the substitution, we obtain the dimensionless Navier-Stokes equation. Assuming no external forces, after some algebraic manipulations we get:

$$(\mathbf{v}' \cdot \nabla') \mathbf{v}' = -\nabla' P' + \frac{\eta}{\rho v_0 L} \nabla'^2 \mathbf{v}' \equiv -\nabla' P' + \frac{1}{\text{Re}} \nabla'^2 \mathbf{v}'. \quad (1.30)$$

Here, the Reynolds number is defined as the ratio of inertial and viscous dissipative forces

$\text{Re} \sim (\mathbf{v}' \cdot \nabla')\mathbf{v}' / \nabla'^2 \mathbf{v}'$ and can be expressed as $\text{Re} = \rho v_0 L / \eta$. From this definition, we can conclude that all flows with the same Re and the same boundary conditions (similar, appropriately scaled geometries) have also the same dynamics, because they are represented by the same dynamical equation.

According to our definition, we can use the Reynolds number as an indicator as to whether or not a given steady flow of classical fluid is laminar or turbulent. In flow past a cylinder, the laminar character is observed when $\text{Re} \sim 1$, and the very first laminar vortices appear in the wake when $\text{Re} \sim 10$. Above this value, the viscous term starts to be much smaller compared to the inertial one and more and more kinetic energy is carried by the vortices.

When $\text{Re} \sim 100$, the so-called *Kármán vortex street* is observed before fully developed turbulence emerges at $\text{Re} > 10^5$ (see in [15]). Here, the viscosity no longer plays any role at large length scales and most of the injected energy is transferred to very small vortices without much dissipation along the way. The kinetic energy is, of course, eventually dissipated by viscous forces acting at the smallest length scales (suppressing the motion of the smallest vortices).

1.8 Drag Forces Acting on Submerged Objects

Let us consider a fluid flowing past a solid object of some arbitrary shape. In the case of a viscous fluid, the *drag force* acting on the bluff body depends on the flow velocity, viscosity and geometry of the object. For example, if we choose laminar flow past a sphere, then the relation for the viscous drag force⁶ is the famous Stokes' law:

$$\mathbf{F}_{\text{lam}} = 6\pi\eta r \mathbf{v}, \quad (1.31)$$

where r is the radius of the sphere and \mathbf{v} is the velocity of the stream at infinity. Relation (1.31) is specific for a sphere, but the proportionality $\mathbf{F}_{\text{lam}} \propto \mathbf{v}$ holds for any arbitrary body. When the Reynolds number is high enough, the drag force (or pressure drag) for a turbulent flow is expressed as:

$$\mathbf{F}_{\text{turb}} = \frac{1}{2} C_D S \rho v^2 \hat{\mathbf{e}}_{\mathbf{v}}, \quad (1.32)$$

where S is the cross-sectional area of the object perpendicular to the flow, $\hat{\mathbf{e}}_{\mathbf{v}}$ is a unit vector pointing in the same direction as \mathbf{v} and C_D is the *drag coefficient*, which is a specific dimensionless number related with the body's geometry. Henceforth, we will describe the fluid motion in terms of the drag coefficient dependence $C_D(v)$ on velocity instead of the force dependence $F(v)$.

⁶This type of drag force is sometimes called *skin friction*.

In summary, the relation for laminar and turbulent (Newton) cases takes the form:

$$C_D \propto v^\alpha, \quad \text{where } \begin{cases} \alpha = -1 & \text{for } \text{Re} \in (0 - 10) \\ \alpha = 0 & \text{for } \text{Re} \in (10^3 - 10^5) \end{cases} .$$

The full dependence of experimentally measured $C_D(\text{Re})$ (for constant density, viscosity and similar sizes of objects) is sketched on the graph below for various geometries.

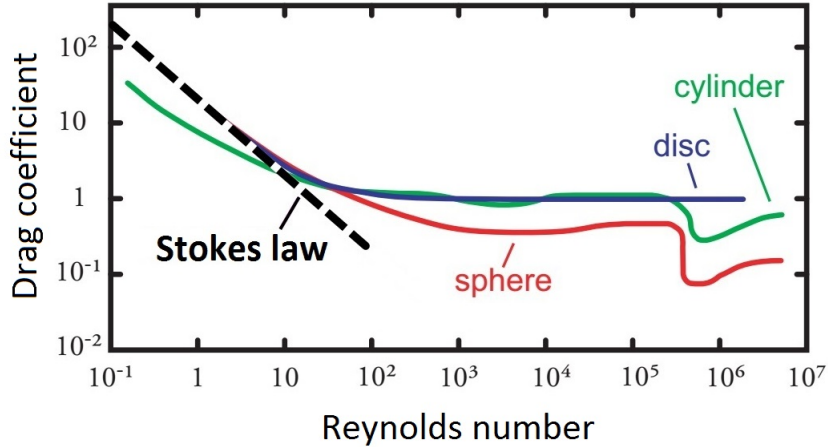


Figure 1.7: Drag coefficient dependence for a thin disc (blue line), cylinder (green line) and a sphere (red line) versus the Reynolds number. In this log-log plot, the laminar drag (black line) is undoubtedly localised within low values of Re with known relation $C_D \propto \text{Re}^{-1}$. Then, at $\text{Re} \in (10^2 - 10^3)$, the pressure drag dominates and $C_D = \text{const.}$ until it suddenly falls down at $\text{Re} \approx 500,000$. This phenomenon is called the *drag crisis*, which states that above the critical value of Re , the boundary layer around the object turns turbulent and therefore, the separation region (the region where the boundary layer detaches from the surface of the bluff body) shifts, reducing the cross-section of the turbulent wake. Note that this does not occur for the thin disc (placed perpendicularly to the flow).

1.9 Oscillatory Motion in a Viscous Fluid

Since this work concerns vibrating objects (tuning forks) in superfluid He-II, we will briefly discuss the theory of oscillatory fluid behaviour.

Penetration Depth

If an infinite xy -plane is submerged in a viscous fluid and harmonically oscillating in x -direction with angular frequency ω , the fluid will also oscillate in the x -direction with the same frequency as the plane does due to viscous forces. However, the dissipative processes will damp the oscillation as we go further from the plane in the z -direction (plane is put at $z = 0$). Hence we are expecting the solution of Navier-Stokes equation (1.29) in the form of $\mathbf{v} = [v_x(z, t), 0, 0]$. The motion equation is in this case much simpler, because the term $(\mathbf{v} \cdot \nabla)\mathbf{v} = 0$, the pressure is constant everywhere $P = \text{const.}$ and gravitational force can be neglected.

For this situation, the solution of Navier-Stokes equation (1.29) is a well-known exponentially attenuated harmonic wave:

$$\mathbf{v} = v_0 e^{i(kz - \omega t)} e^{-z/\delta} \hat{\mathbf{e}}_z, \quad (1.33)$$

where $k = 1/\delta$ is the wave number, and δ is the *penetration depth*. Beyond this distance, the fluid oscillation is damped stronger than e -times, so δ becomes the characteristic dimension of the damped wave. It is given as[4]:

$$\delta = \sqrt{\frac{2\eta}{\rho\omega}}. \quad (1.34)$$

The penetration depth decreases with frequency, meaning that for high-frequency oscillations, the fluid oscillations are confined to the vicinity of the oscillating plane.

Oscillatory Reynolds Number

Because of the extra degree of freedom in oscillatory flow (the period of oscillation), one dimensionless parameter such as Re , as defined for steady flow, cannot fully describe the flow. Hence, two dimensionless numbers are generally needed.

However, in the special case of the *high-frequency limit* ($\omega > 2\eta/\rho L^2$) the situation is simplified. If the penetration depth δ becomes significantly smaller than all other relevant dimensions such as body size or surface roughness, then L should be replaced by δ in the process of scaling the Navier-Stokes equation. This is because one of the points of the scaling is to estimate the magnitudes of velocity derivatives in the flow field and we have to take the largest values available. From this re-scaling of the NS equations it follows that in the high frequency limit, all relevant quantities can be again combined into a single dimensionless parameter – the oscillatory Reynolds number Re_δ . Using (1.34) we obtain:

$$Re_\delta = \frac{v_0 \delta \rho}{\eta} = v_0 \sqrt{\frac{\rho}{\eta \pi f}}. \quad (1.35)$$

1.10 Oscillations in Superfluid He-II

So far, have only considered oscillations in a classical fluid. To apply the theory to two-fluid model, we have to make adjustments so that it will work for both the normal and superfluid component.

When a high-frequency oscillating body with low velocity amplitude is submerged in superfluid He-II, the drag force is expected to be caused only by the viscous forces of the normal component. However, the density ρ_n of this component decreases with temperature

(as introduced in **Section 1.2, Figure 1.2**) and we are forced to work with the characteristic penetration depth δ_n and oscillatory Reynolds number Re_n :

$$\delta_n = \sqrt{\frac{2\eta}{\rho_n \omega}}, \quad Re_n = \frac{v_0 \delta_n \rho_n}{\eta}. \quad (1.36)$$

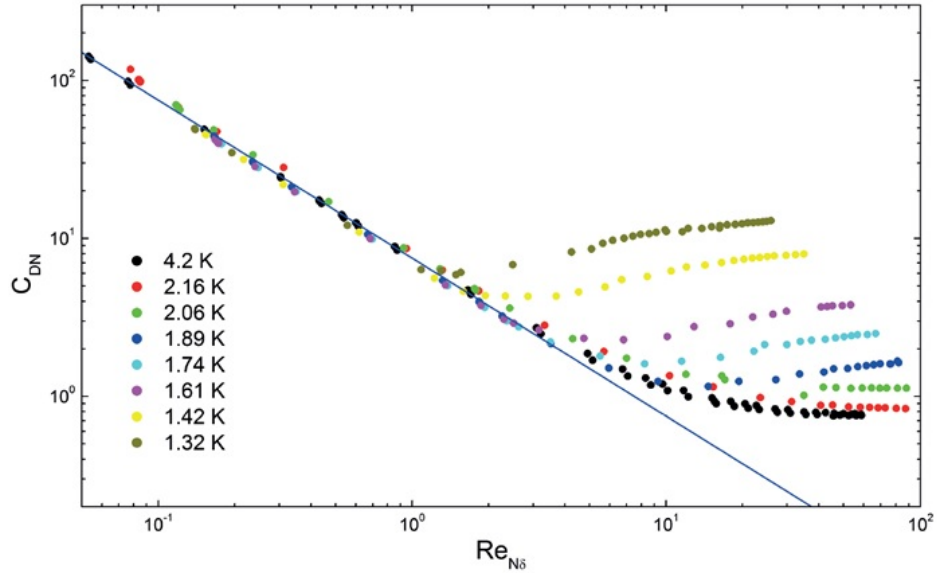


Figure 1.8: Number of experiments made a few years ago show that the definition of oscillatory Reynolds number in superfluid ${}^4\text{He}$ (1.36) is chosen correctly since all curves lies on the same place within the laminar range and in turbulent differs only by the presence of QT.

Motivation

The drag coefficient for objects submerged in classical fluids have been explored already. The process and conditions for making the turbulence have been intensively studied for various-shaped objects and wide range of oscillation frequencies.

Because of two-fluid behaviour of He-II, two types of turbulence may occur when an immersed body oscillates - classical and quantum. The first one is an ordinary turbulence caused by the normal component and described by the oscillatory Reynolds number Re_δ . The second, quantum turbulence consists of quantized vortices, for which the complete theoretical description and sufficient number of experiments are still missing, but there are hints that the relevant physical quantity governing vortex nucleation is a critical velocity, which is expected to scale as $\sqrt{\omega\kappa}$ [16], where ω is angular frequency and κ the circulation quantum.

We already know that vortex nucleation can be launched if the normal component or a submerged body moves at a high enough velocity relative to the superfluid component, but to this day, experiments are missing that would clearly prove whether both turbulences form simultaneously or not. In this work we present measurements showing that classical and quantum turbulence can form independently.

2. Experimental Setup

The whole experimental system consisted of a QT generator and two second sound sensors, which were placed into a cylindrical resonator cavity of diameter $d = 10\text{ mm}$ and height $H = 65\text{ mm}$. One of the second sound sensors (speaker) is connected to the waveform generator and the other one (receiver) to a SR-830 lock-in amplifier. A more detailed description is presented later in this chapter.

2.1 Quantum Turbulence Generator

Quantum turbulence can be produced by any oscillating objects such as grids, tuning forks or spheres. In our experiment we used an oscillating piezoelectric tuning fork, fully controlled electrically.

Quartz Tuning Fork

In general, quartz tuning forks are commercially produced piezoelectric oscillators. Their most common application is as frequency standards in digital watches or other electronic components. We used a custom-made fork with fundamental resonance at $f_0 = 6500\text{ Hz}$ in vacuum at room temperature. The geometry of the fork is sketched in **Figure 2.1**.

The size of the fork is given by prong length $\mathcal{L} = 3.5\text{ mm}$, prong width $\mathcal{W} = 75\mu\text{m}$, thickness $\mathcal{T} = 90\mu\text{m}$ and the distance between prongs $\mathcal{D} = 90\mu\text{m}$. The fork was driven by an amplified alternating voltage $U \propto e^{i\omega t}$, causing the anti-phase lateral oscillation of fork's prongs. The first flexural overtone can be found at the frequency $f_1 = 40\text{ kHz}$. In this resonant mode, there are two nodes and anti-nodes along the length of the prongs (one anti-node is at the supporting base). In both cases there is an upper boundary for the amplitude of AC voltage. Exceeding this value will cause the prongs to hit each other repeatedly, which could result in serious damage.

Two other important properties of fork are the effective mass of one prong m_{eff} and a so-called fork constant a . For our case, we can estimate them (using formulas and data from[17, 18]) as:

$$m_{\text{eff}} = \frac{1}{4} \mathcal{L} \mathcal{T} \mathcal{W} \rho_q = 1.52 \cdot 10^{-8} \text{ kg},$$

$$a_{\text{fund}} = 3.61 \cdot 10^{-7} \text{ Cm}^{-1},$$

$$a_{\text{over}} = 1.38 \cdot 10^{-6} \text{ Cm}^{-1},$$

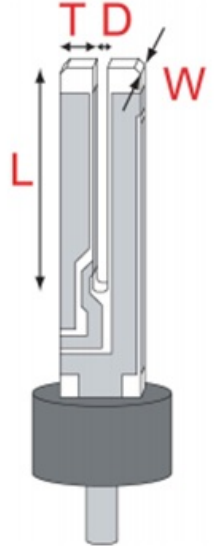


Figure 2.1: Sketch of quartz tuning fork.

where $\rho_q = 2650\text{ kg/m}^3$ is the quartz density. Values of the fork constants were taken from[18], where tuning forks of the same parameters and from the same series were used.

It was also shown[17] that by applying AC voltage with amplitude U_A results in a driving force acting on the fork's prongs of magnitude $F = \frac{1}{2}aU$. Moreover, by measuring the current response I we can determine the velocity at the tip of the prongs as $v = I/a$. Knowledge of these parameters is crucial for all measurements related with superfluid hydrodynamics.

2.2 Second Sound Source and Detector

Second sound is a wave of temperature and entropy, but can be produced purely mechanically. In particular, when a semi-permeable membrane with sub-micron pores is oscillating in He-II, the superfluid component can flow through the pores much easier than the normal component (due to the lack of viscosity). Thus, its oscillation will push only the normal component and consequently, this creates (due to continuity equations) a local oscillation of densities ρ_n , ρ_s and hence, a longitudinal wave of second sound. At the right frequency of oscillation, this results in a resonant second-sound standing wave in the experimental cylindrical cavity.

In our experiment we used two identical sensor devices to produce and also detect the second sound. The sensor itself is essentially a capacitor where one electrode consists of the membrane with a 100 nm thick gold layer above the surface and the other electrode is made of brass. The full sketch and photo can be seen in **Figure 2.2**.

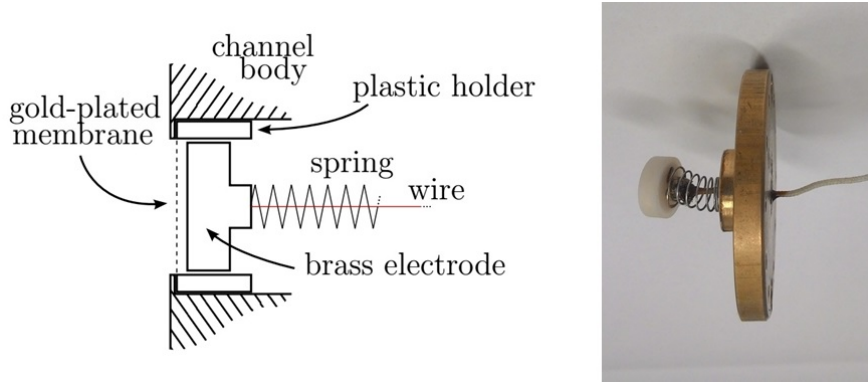


Figure 2.2: Left: Technical sketch showing the parts of the second sound sensor. Right: A photograph of our experimental construction.

The gold electrode is electrically connected with the resonator body while the other electrode to the wave generator or lock-in amplifier (depends whether the device is set as a speaker or receiver). Together, these electrodes form a capacitor of $\approx 60 - 100$ pF and applying an AC voltage (units of Volts) superimposed on a 90 V DC bias causes the oscillation of the membrane and therefore production of second sound.

Because of finite distance between the sensors H , we observe many harmonic resonance modes. The resonance frequency can be estimated from the equation for standing waves:

$$f = \frac{u_2}{\lambda} = \frac{u_2}{2H}n . \quad (2.1)$$

2.3 The Apparatus

We have introduced the principle of making quantum turbulence and also its detection. In this section we describe the necessary technical parts of the experiment in more detail.

Resonator

As mentioned above, the quartz tuning fork and both second sound devices were placed into the cylindrical resonator cavity. The fork is located in the middle and the second sound sensors at each end of the resonator, facing each other.

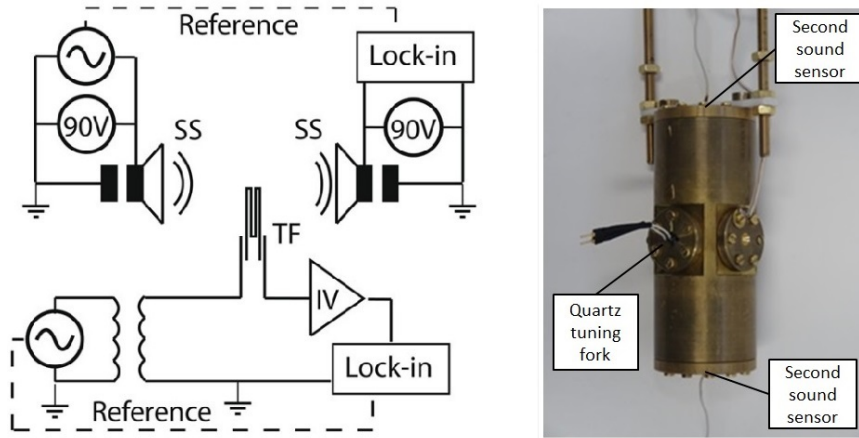


Figure 2.3: Left: Electrical schematics of the setup. Right: Photograph of the resonator.

A small 1 mm thin hole is drilled through the body, connecting the cavity to the open bath filled with superfluid helium.

Insert

To ensure a fixed location of the resonator inside the helium bath, we attached it at the bottom of the *insert*. The cryogenic insert is a large metallic construction, to which all resistors, coaxial cables, and thermometers are attached. The total height of insert is comparable with the height of the cryostat, so when placed into a superfluid bath, the resonator will be located near the bottom. Since the helium level in cryostat is continuously decreasing, this location of resonator is optimal.

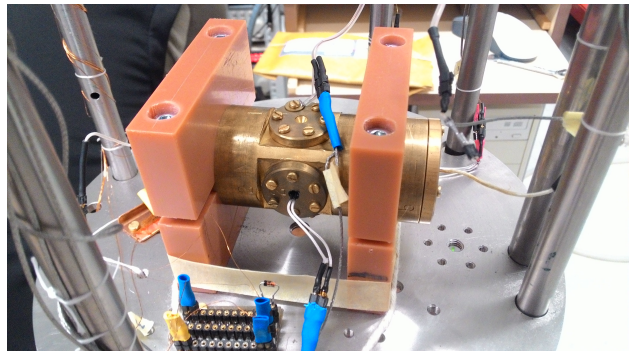


Figure 2.4: Photograph of the resonator fixed at the bottom of the insert.

Cryostat

The insert along with all important devices were put into a vessel, designed for working with cryogenic fluids. At the top, the cryostat allows access into the helium bath, but at the same time, the cryostat must be well-insulated from external heat fluxes.

After the cryostat was pre-cooled to liquid nitrogen (LN_2) temperature ($\approx 77\text{ K}$), we continued precooling with helium vapour and finally transferred liquid helium (LHe) at ($\approx 4.2\text{ K}$) from a transport dewar. Vapours from the rapidly evaporating LHe were immediately pumped by a set of Roots-pumps so that the inner pressure above the LHe surface was further decreased. Reducing the saturated vapour pressure provided the cooling even below T_λ . This method works efficiently until the minimum temperature of $\approx 1.25\text{ K}$ is reached.



Figure 2.5: Photograph of the experimental setup - Left: waveform generators, lock-in amplifiers. Middle: cryostat, pipes where helium gas is flowing out of the system. Right: Roots-pump.

During the measurements it was crucial to have the temperature stabilized minimal deviations. Two methods have been used for measuring the temperature. The first was a direct resistance measurement of a miniature semiconductor thermometer (Germanium thin film on GaAs substrate) placed in the helium bath, with calibration known from previous experiments. The second method was a simple conversion between saturated vapour pressure and temperature based on [19]. The pressure was regulated (both manually and electronically) by manipulating the pump valve.

To summarize, we prepared a cooling system able to reach any temperature above $\approx 1.25\text{ K}$. Overall, we did systematic measurements at 9 different temperatures: 2.15 K, 2.05 K, 2.00 K, 1.95 K, 1.80 K, 1.65 K, 1.60 K, 1.55 K, 1.35 K. Although our total temperature range is less than 1 K, there are dramatical changes in the composition of LHe. One can recall (graph in **Figure 1.3**) that at 2.15 K there is only about 5% of the superfluid component and at 1.35 K it is more than 90%.

2.4 Measurement Methods

Since we decided to focus on various aspects of the studied problem, we used several methods of measurement with the quartz tuning fork and second sound sensors, discussed in the following text.

Frequency Sweeps of the Tuning Fork

In this mode the tuning fork was oscillating with a frequency that was changing along some chosen range. This was important for characterizing the fork resonance with its frequency f_0 , width Δf , signal amplitude U_0 and background signal (offset) U_{off} . Frequency sweeps were made around the fundamental and overtone resonance frequencies $f_0^{\text{f}} = 6.38 \text{ kHz}$, $f_0^{\text{o}} = 40.00 \text{ kHz}$. Two examples of these measurements are shown in **Figure 2.6**.

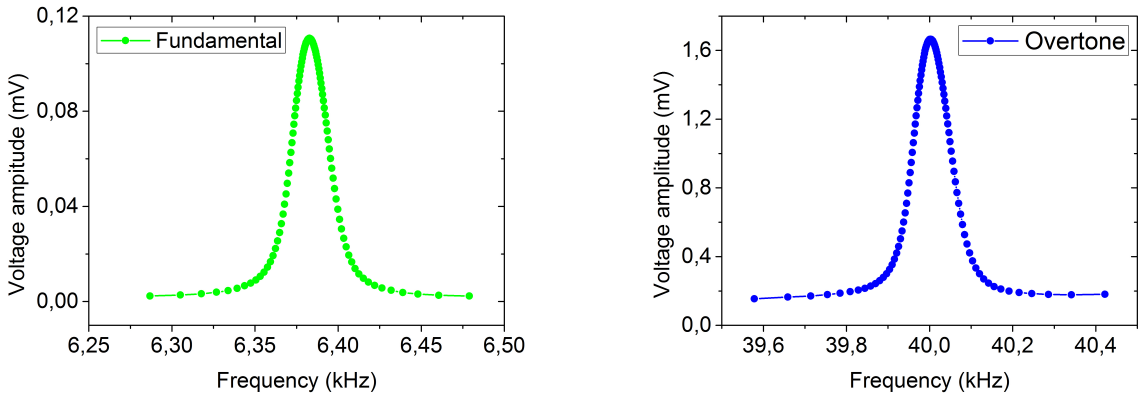


Figure 2.6: Left to right: Fundamental and overtone frequency sweeps.

The fitted full lines are Lorentzian curves with the general formula from [17]:

$$U(f) = U_{\text{off}} + U_0 \frac{(\Delta\omega)^2 \omega^2}{(\omega^2 - \omega_0^2)^2 + (\Delta\omega)^2 \omega^2}. \quad (2.2)$$

During this measurement the time step was set to 100ms and adaptive sampling was used due to the fact that we are more interested in the data-points sitting on the curve than outside. These frequency sweeps have been measured every time we changed the temperature or driving voltage because of possible resonant frequency shifts.

Frequency Mode for Second Sound

The distance between the speaker and receiver is $H = 54 \text{ mm}$ and the second sound velocity is approximately $u_2 \approx 20 \text{ m/s}$ within the range of temperatures (1.35 K – 1.95 K). Using Eq. (2.1) we can estimate the second sound 1st resonant mode as $f = u_2/2H \approx 185 \text{ Hz}$.

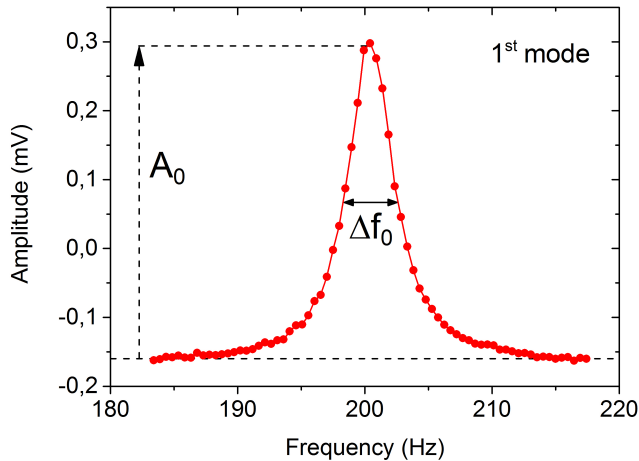


Figure 2.7: 1st harmonic mode of second sound. Peak height A_0 and width Δf_0 are important parameters when inferring the vortex line density.

The observed 1st resonance mode frequency slightly differs from the estimated one, due to finite lateral dimensions and non-ideal geometry. Additionally, this mode is most sensitive in the middle of resonator, where the fork is located. Therefore, all the measurements including second sound were made at the 1st mode.

Constant Drive of Tuning Fork and Second Sound

In this mode, the second sound ran continuously on its 1stresonance mode whilst the fork oscillated also at its resonance (fundamental or overtone).

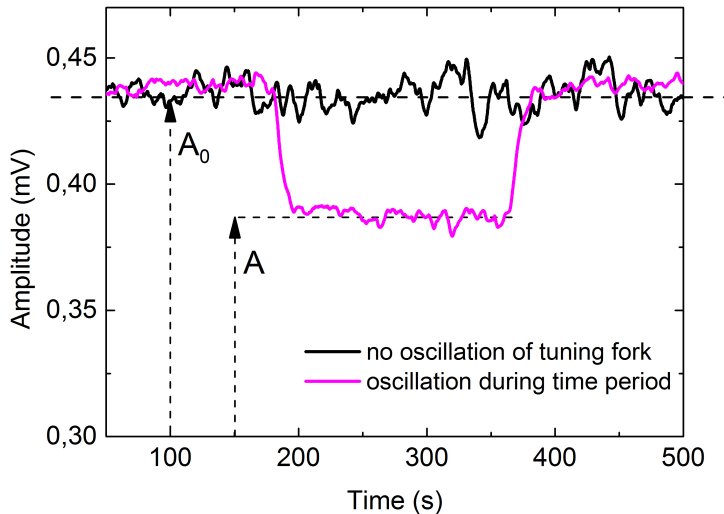


Figure 2.8: An example of suppressed second sound signal when the fork starts to oscillate. Time on the x-axis is measured since the execution of the measurement software. $A_0 - A$ corresponds to the signal drop, related to the equation of quantum turbulence 1.26.

3. Results

Here we present the experimental data obtained from the measurements of quantum turbulence. The tuning fork has been immersed in superfluid ^4He and forced to oscillate at two, geometrically different (in the sense of different velocity profile along the fork's prongs) modes - *fundamental* [6380 Hz] and *overtone* [40 000 Hz].

The first part of this chapter is focused on the measurement of vortex line density L (total length of vortices in unit volume) using the second sound attenuation technique. We will try to find the conditions for production of quantized vortices and also, quantify their amount.

In the second part we will work only with the tuning fork via the applied voltage amplitudes and its current responses. Using the scaled drag coefficient and oscillatory Reynolds number, we will be able to estimate when the drag force acting on the tuning fork becomes non-linear with velocity. This event is a distinct sign of the flow pattern changing from simple laminar flow of the normal component and purely potential flow of the superfluid component, to something more complex involving some form of classical and/or quantum turbulence.

Overall we worked at seven selected temperatures in the two-fluid regime, when both superfluid and normal component amounts are considerable: 1.35 K, 1.55 K, 1.65 K, 1.80 K, 1.95 K, 2.05 K, 2.15 K. **Figure 3.1** shows the time trace of the temperature inside the cell. Temperatures below ≈ 1.30 K were not stable, so the lowest fixed value was set to 1.35 K.

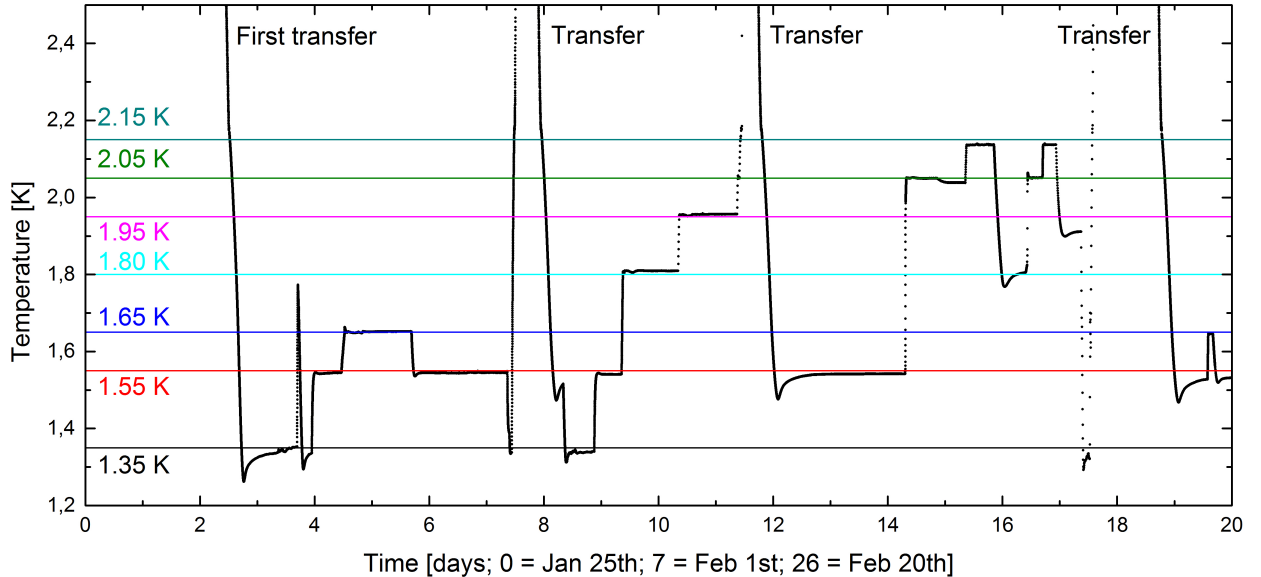


Figure 3.1: Record of the temperature inside the cryostat. Due to strong evaporation of superfluid helium and relatively long durations of the measurements at each temperature, we had to refill the cryostat three times. Unfortunately, this may have caused some unsystematic behaviour of the tuning fork that manifested after the first refill on Day 8, see the text for details.

Due to the prolonged experimental times, we had to refill helium three times, which has likely contributed to unsystematic behaviour of the tuning fork. The fork has yielded different results at the same temperature before and after transfers, especially the refill on Day 8.

The data presented in this Thesis should thus be considered as if consisting of two separate categories of measurements: (i) temperatures 1.35 K, 1.55 K, 1.65 K investigated before Day 8; and (ii) remaining higher temperatures investigated after said transfer. Where we had the choice, we chose to present data measured before the transfer, as we believe that these better reflect the actual properties of the tuning fork and are more useful for comparison (e.g. they compare better with Ref. [20]). Similar effects in terms of different behaviour after the refilling have been observed with other oscillators such as vibrating wires [21].

We believe that the most likely scenario is that during the transfer and subsequent cooling, some small amount of air entered into the helium bath, solidified, and despite the protection offered by the resonator body, some bits of frozen air found their way towards the surface of the fork and were deposited there. Consequently, the altered tuning fork geometry could have affected the helium flow, especially the exact moment when the drag force becomes non-linear due to a flow instability. While this unfortunate event means that we are, in principle, working with two different oscillators rather than the exact same tuning fork at all of the investigated temperatures, we believe that the vortex line density measurements correlated with the drag forces acting on the tuning fork still provide very interesting results and are highly valuable not only as a basis for further studies and improvements, but also directly, as a study of oscillatory flows in superfluid helium (regardless of the exact geometry of the vibrating object).

3.1 Measurement of Vortex Line Density

It has already been shown that an object oscillating with sufficient velocity can produce quantized vortices in superfluid helium. For this purpose, we used the tuning fork mounted in the second sound resonator. Our measurement protocol is given in the following steps:

- 1) First, after the desired temperature in the cryostat has been reached, we run the frequency sweep on tuning fork and second sound independently. The tuning fork frequency sweeps are repeated at different drive levels. This gives us the necessary information about the resonance frequencies and widths.
- 2) Next we set up the second sound sensors in constant drive mode at its fundamental resonance and allow up to 3 minutes for stabilization.
- 3) When this time has passed, we also run the tuning fork in constant drive mode at its resonance (fundamental or overtone) with a given voltage amplitude U_0 for 3 minutes.
- 4) The tuning fork is subsequently turned off and the second sound is again left to stabilize for 2 minutes.
- 5) The values of A and A_0 were taken as averages of the periods when the tuning fork was on and off (cutting the transients), respectively (see **Figure 3.2**).

The five aforementioned steps were repeated for several values of voltage applied across the tuning fork, for both fundamental and overtone mode at all six temperatures (all of

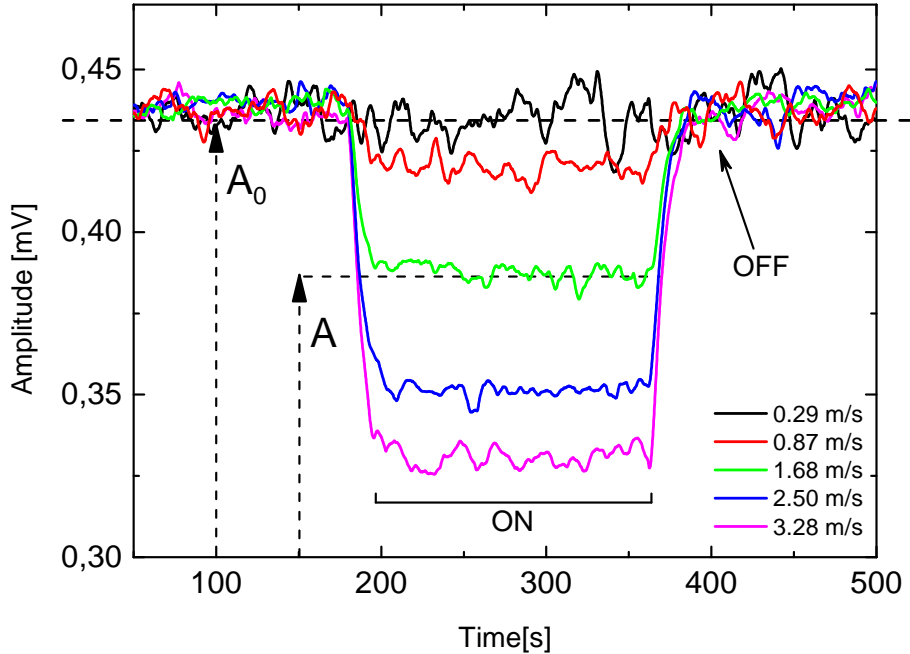


Figure 3.2: An example of second sound attenuation due to the presence of quantized vortices, produced by an oscillating tuning fork at various velocities. "ON" and "OFF" labels describe the state of the tuning fork. The time on the x-axis is measured from the beginning of each particular run. Values shown in this graph are taken at the temperature $T = 1.95$ K. The measurement at the velocity of 0.29 m/s corresponds to a vortex line density $L_0 = 3 \times 10^6 \text{ m}^{-2}$ and is taken as an estimate of the sensitivity threshold of our measurement technique.

the above except 1.65 K). We have always proceeded from low values of driving voltage to higher ones gradually, so that it is clear, at which point any measurable amount of quantum vortices appears.

By collecting datasets of A , A_0 and Δf_0 we could estimate the vortex line density L :

$$L = \frac{6\pi\Delta f_0}{B\kappa} \left(\frac{A_0}{A} - 1 \right), \quad (3.1)$$

and the fork tip velocity $v = I/a$, where I is current response and a the fork constant. The resulting plot (**Figure 3.3**) is shown below.

We should point out that the results for L as derived in **Section 1.6** are valid only for homogeneously and isotropically distributed vortices. The amount of quantized vortices is expected to be higher near the fork than further away from it. Since we utilized the 1st second sound resonant mode, we have, in fact, measured the 1st Fourier component of the vortex line density spatial distribution[22]. This is sufficient for the purposes of (roughly) estimating the quantities of quantized vortices produced, but the true values of L near the tuning fork may differ by some factor and could be obtained only by measurements using several additional second sound resonant modes.

Nevertheless, from **Figure 3.3** we observe that no significant amounts of vortex lines are produced before a certain critical velocity is exceeded. Furthermore, we find that the amount

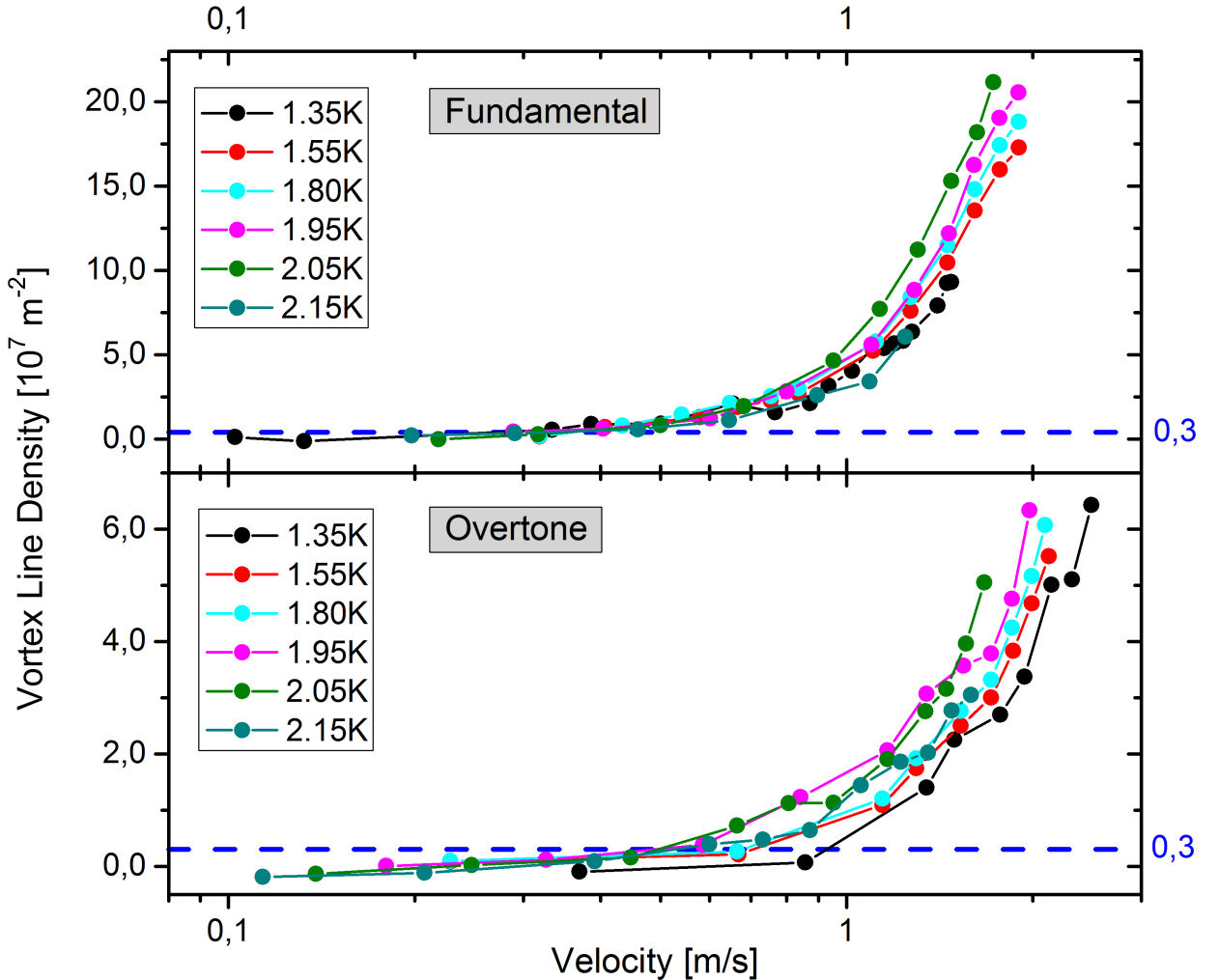


Figure 3.3: Vortex line density L against the (logarithmically scaled) peak velocity of the tuning fork v . The blue dotted line marks the threshold level $L_0 \approx 3 \cdot 10^6 \text{ m}^{-2}$ introduced in **Figure 3.2**, above which the measured vortex line density can be regarded as reliable.

of quantized vortices produced is temperature-independent and scales only with the velocity of the tuning fork.

Plotting L on a logarithmic scale we observe (see **Figure 3.4**) that the critical velocities, above which the quantum vortices are produced in much larger amounts, are also independent of temperature. Bearing in mind the sensitivity threshold, we estimate these critical velocities for the fundamental and overtone modes to be $v_c^f = 0.3 \pm 0.1 \text{ m/s}$, and $v_c^o = 0.7 \pm 0.2 \text{ m/s}$, respectively. Moreover, as noticed in **Section 1.10**, the critical velocity should scale with frequency as $\propto \sqrt{\kappa\omega}$. From our results we get $v_c^f/v_c^o \cdot \sqrt{f_0^o/f_0^f} \doteq 1.06$, which is consistent with the given scaling.

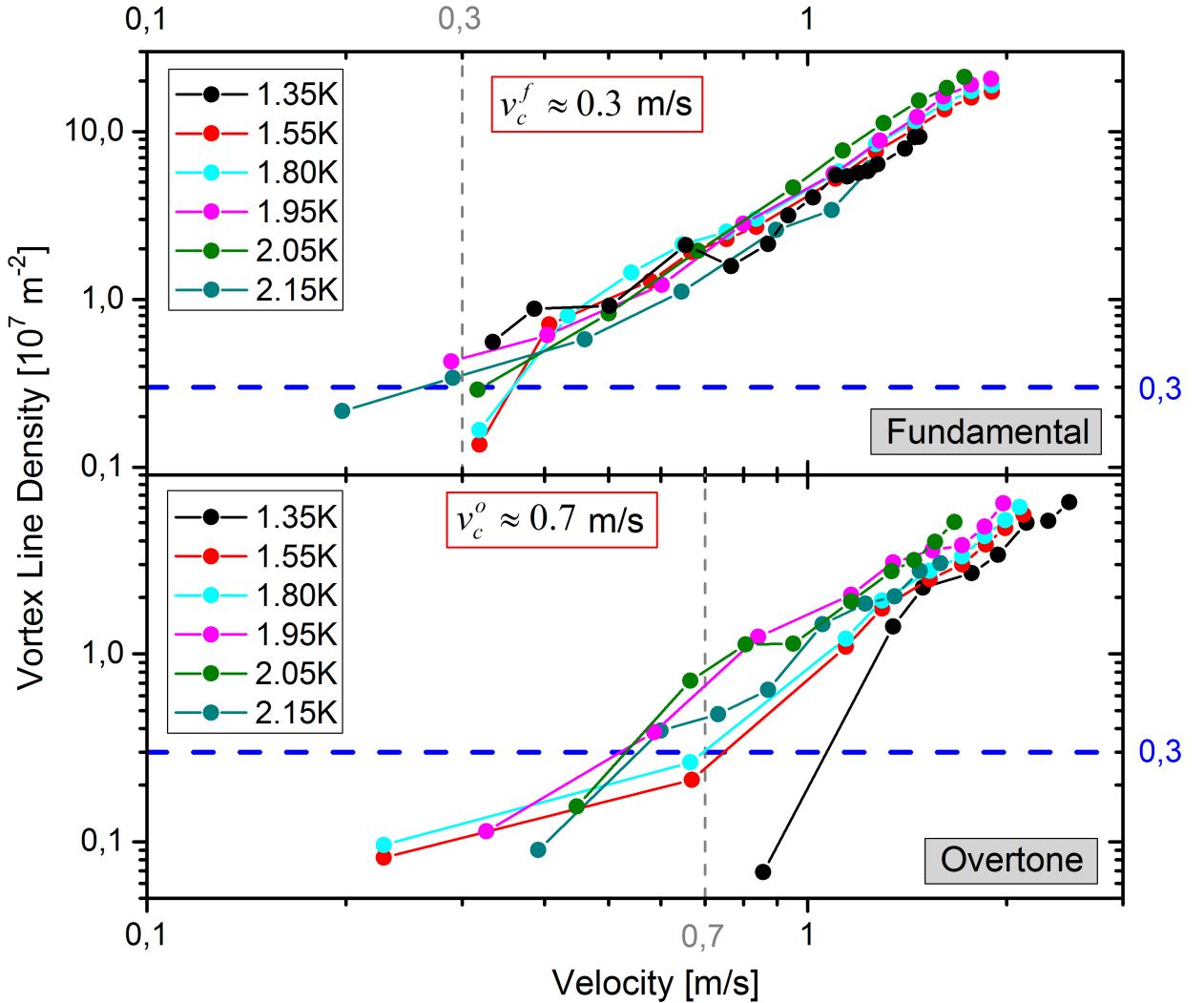


Figure 3.4: Log-log graph of the vortex line density L against the peak velocity of the tuning fork (the same data as in **Figure 3.3**). This graph better illustrates the position of threshold $L_0 \approx 3 \cdot 10^6 \text{ m}^{-2}$ (blue dashed lines) and the temperature-independent critical velocities (grey dashed lines). The tuning fork peak velocity is determined with an uncertainty of about 10% that arises from the electrical calibration procedure[23]. The vortex line density is affected by a systematic error that is mainly due to the assumption of a homogeneous isotropic tangle in deriving (3.1) that obviously does not correspond to the vortex tangle produced in the vicinity of the tuning fork.

Increasing the sensitivity of the second sound measurement (and thus lowering the threshold level) would allow determining the critical velocities with better accuracy and reduce the scatter in the observed data. Although the design of the second sound resonator and sensors is far from perfect, the current sensitivity is sufficient for a qualitative discussion of the relationship between the obtained vortex line densities and the drag forces acting on the tuning fork.

3.2 Drag Force Measurements

All of drag force measurements presented in this Section were done solely with the tuning fork; second sound was not used during the measurement. We have operated the tuning fork in full frequency sweeps, with gradually increasing/decreasing driving voltages. Each of the datapoints in the following graphs is thus obtained from a full frequency sweep of tuning fork around its fundamental or overtone resonance frequency with a given applied voltage U_0 . From such a sweep, the current response I was measured and for each pair $[U_0, I]$ we found the corresponding values of peak applied force and peak velocity $[F, v]$ using the calibration formulae from [17]: $F = aU_0/2$, $v = I/a$.

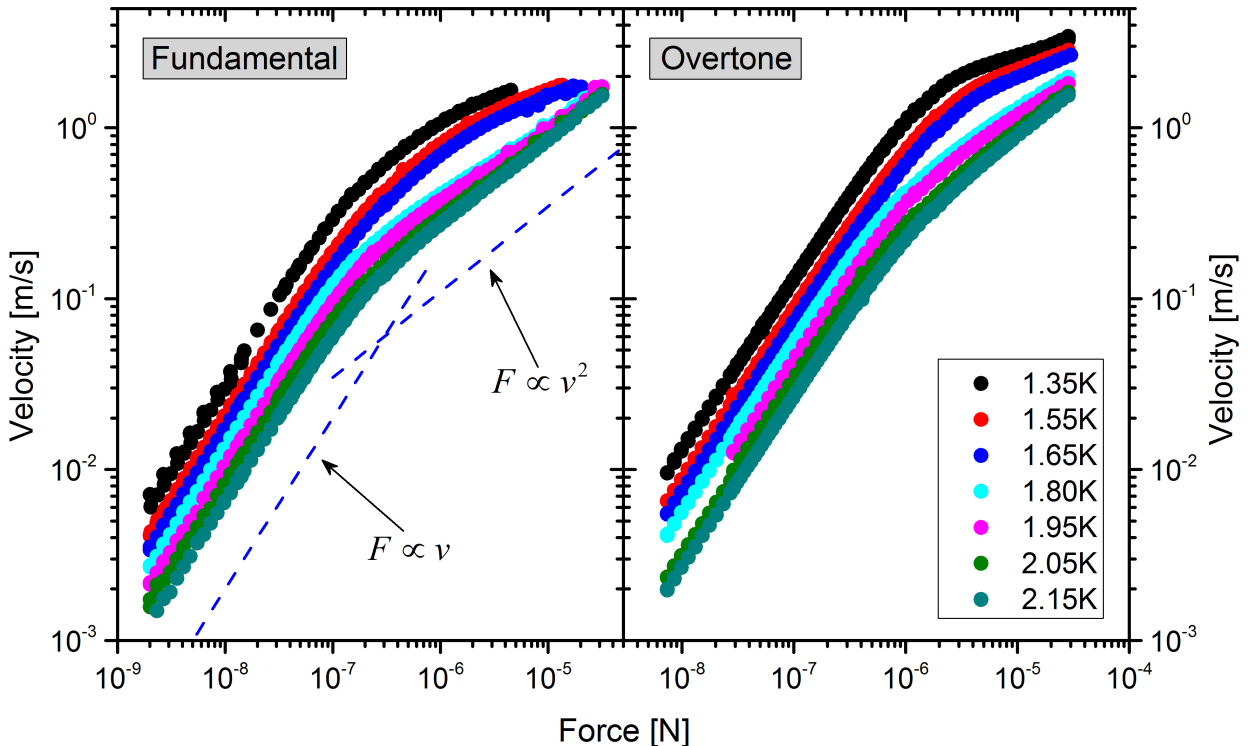


Figure 3.5: Force-Velocity characteristics for the fundamental and overtone modes of our tuning fork at seven different temperatures spanning the two-fluid regime. Apparently, a transition from linear to non-linear drag force occurs at high enough velocities. The *blue dotted lines* sketch the approximate theoretical dependencies for laminar and classical turbulent flow.

In **Figure 3.5** a transition from linear to non-linear drag is clearly observed. In classical fluid mechanics, the onset of force non-linearity is interpreted as a formation of a wake past the bluff body that encompasses vortical motion of the fluid and may eventually lead to the generation of turbulence. Our case is more complicated since we deal with two (possibly interacting) fluids and hence with two mutually-dependent types of turbulent motion.

It is also apparent that the linear drag force strongly depends on temperature, which reflects the fact that only the normal component contributes to the drag force in laminar flow. At the same time, the superfluid component exhibits purely potential flow, as an ideal fluid might, which results in a zero net contribution to the drag force as per d'Alembert's paradox [4]. To discuss the scaling properties in greater detail, it is, however, necessary to convert

the force and velocity into relevant dimensionless quantities, such as the drag coefficient $C_D = 2F/S\rho v^2$ and the oscillatory Reynolds number $\text{Re}_\delta = v\rho\delta/\eta$, , where S stands for the cross-section area of fork perpendicular to the direction of oscillation and F for the measured drag force.

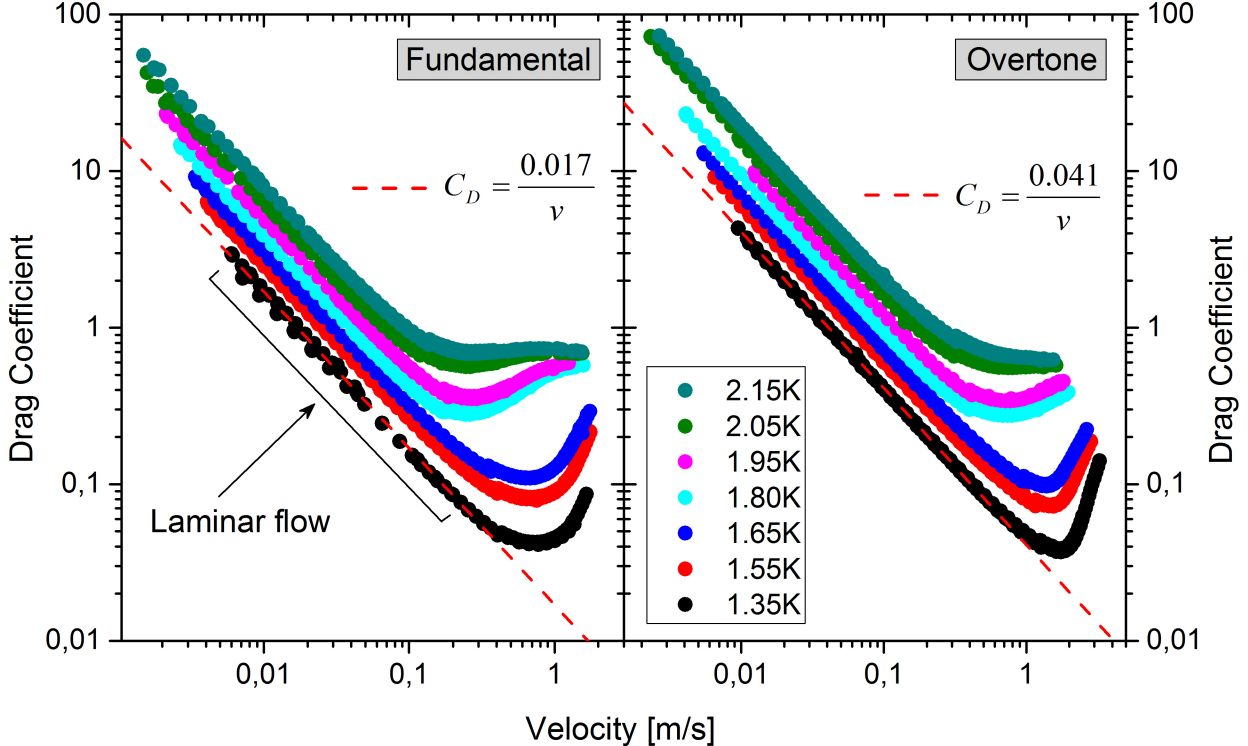


Figure 3.6: Drag coefficients plotted against the peak velocity of the oscillating tuning fork. The *red dotted lines* fit the laminar part of the dependences for the temperature 1.35 K, with different values of the fitting parameter for the two tuning fork modes.

Looking at the graph in **Figure 3.6** we can recognize “two types” of curves. Those for which the non-linearity seemingly appears at one certain velocity, and those for which the onset arises when exceeding different velocities. This can be regarded as the first sign that either quantum turbulence (QT) or classical turbulence (CT) may occur first under different conditions. Moreover, we note that the 2.15 K curve seems to approach the dependence of the drag coefficient as we know it from classical fluids, with the limiting constant value not far below $C_D = 1$, which is expected for tuning forks in a classical fluid [24].

Within the two-fluid model, we distinguish between the drag coefficient and oscillatory Reynolds number for the whole fluid C_D , Re_δ and only for the normal component alone $C_{Dn} = 2F/S\rho_n v^2 = C_D \rho / \rho_n$, $\text{Re}_{\delta_n} = v \rho_n \delta_n / \eta_n$. For each temperature, the values for the density of normal component ρ_n and dynamical viscosity were taken from [19].

The resulting graph (**Figure 3.7**) showcases three interesting and important facts. First, within the laminar range, all curves collapse to a single dependence, confirming the validity of the scaling proposed in **Sections 3.3, 3.4** and establishing the oscillatory Reynolds number as a suitable dimensionless parameter. Second, for both modes, the laminar part could be fit by the exact same straight line. This represents the fact that the drag force scaling in the high-frequency regime is, with all likelihood, independent on the velocity profile along the

prong and holds even for frequencies differing by a factor of $40\,000/6380 \approx 6.27$. Finally, the critical Reynolds number for generating classical turbulence within both fork modes (the 2.15 K curve best shows) has been estimated as $\text{Re}_{\delta_{nc}} = 7 \pm 2$.

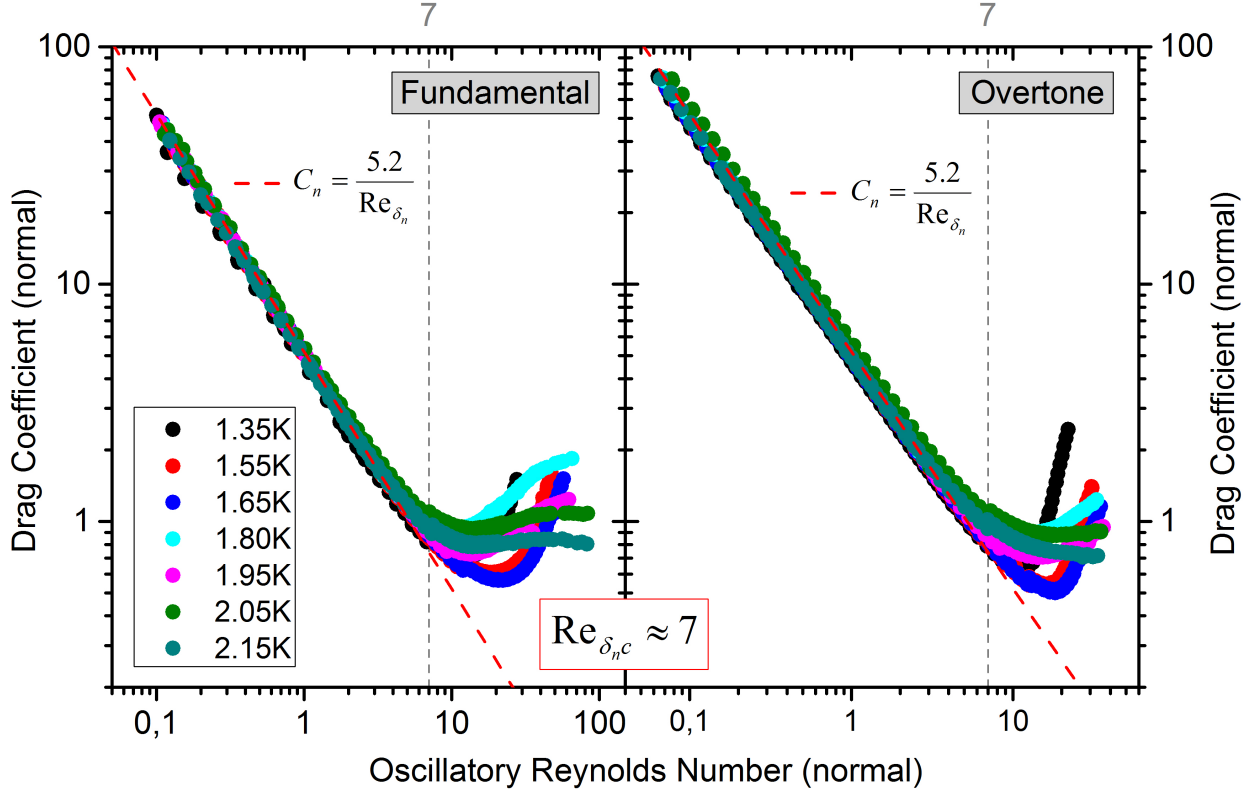


Figure 3.7: Drag coefficient plotted against the oscillatory Reynolds number, both evaluated for the normal component alone. Statistically, the onset of non-linear drag occurs for all temperature curves within the interval $\text{Re}_{\delta_n}^{\text{crit}} = 7 \pm 2$. The presented data are, however, affected by the observed unsystematic behaviour of the tuning forks with regard to the onset of non-linear drag, as discussed in the accompanying text. The *red dotted line* shows the fit of the laminar regime, which is exactly the same for both modes.

At this point, we have to remind the reader that during the actual experiment, we have observed unsystematic behaviour of the tuning forks and therefore the data shown here is very likely affected by this issue. In drag force measurements, this manifested in such a manner that the onset of non-linear drag occurred at different values of Re_{δ_n} when the same temperature was studied at different points during the entire experiment. Therefore, the estimated critical value of $\text{Re}_{\delta_{nc}} = 7 \pm 2$ ought to be taken with some reservations, as it corresponds only to a subset of the acquired data (the four higher temperatures), for which we have reasonable grounds to claim that no significant change of the tuning fork behaviour occurred in between the measurements. Nevertheless, the actual critical value (incorrect as it may be) has little bearing on the interpretation presented below, and we choose to use this particular value as it still describes the majority of the data with a good degree of accuracy.

3.3 Correlation of Results

In the following, we connect the results of vortex line density measurement and the non-linear behaviour of drag coefficient. We will be able to distinguish between quantum turbulence (QT), caused by the presence of quantized vortices and classical-like turbulence (CT) of the normal component. Within this Section, we work only with the fundamental mode.

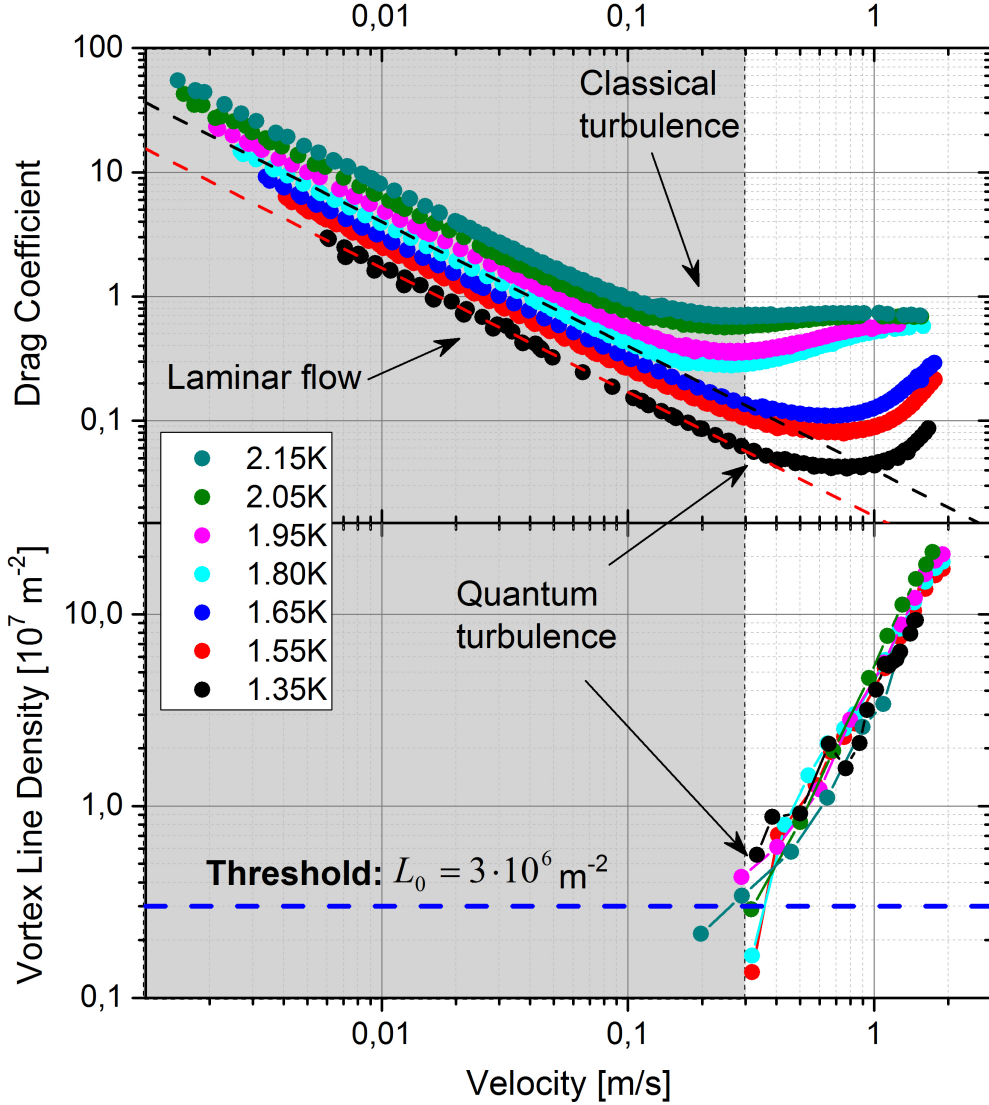


Figure 3.8: Velocity dependence of drag coefficient C_D and vortex line density L for the fundamental mode of the tuning fork. The *blue, red and black dotted lines* are the threshold level and laminar drag fits for 1.35 K and 1.80 K curves, respectively. The *shaded zone* marks sub-critical velocities from the point of view of detection of quantized vortices by second sound, and corresponds to the laminar drag regime for the lowest three temperatures.

In **Figure 3.8** we clearly see the correlation between the production of QT (lower graph) and the onset of non-linear drag force in 1.35 K, 1.55 K and 1.65 K curves. For the other curves (1.80 K and above), the density of normal component is much higher and consequently the critical oscillatory Reynolds number was exceeded earlier than the critical velocity v_c^f .

However, from **Figure 3.8** we are not sure, whether QT really occurred first or CT was just too weak to be noticed by our devices. The graphs in **Figure 3.9** compare the normal drag coefficient C_{Dn} and vortex line density L against Re_{δ_n} and better illustrate the situation. We purposely zoomed the region near transition.

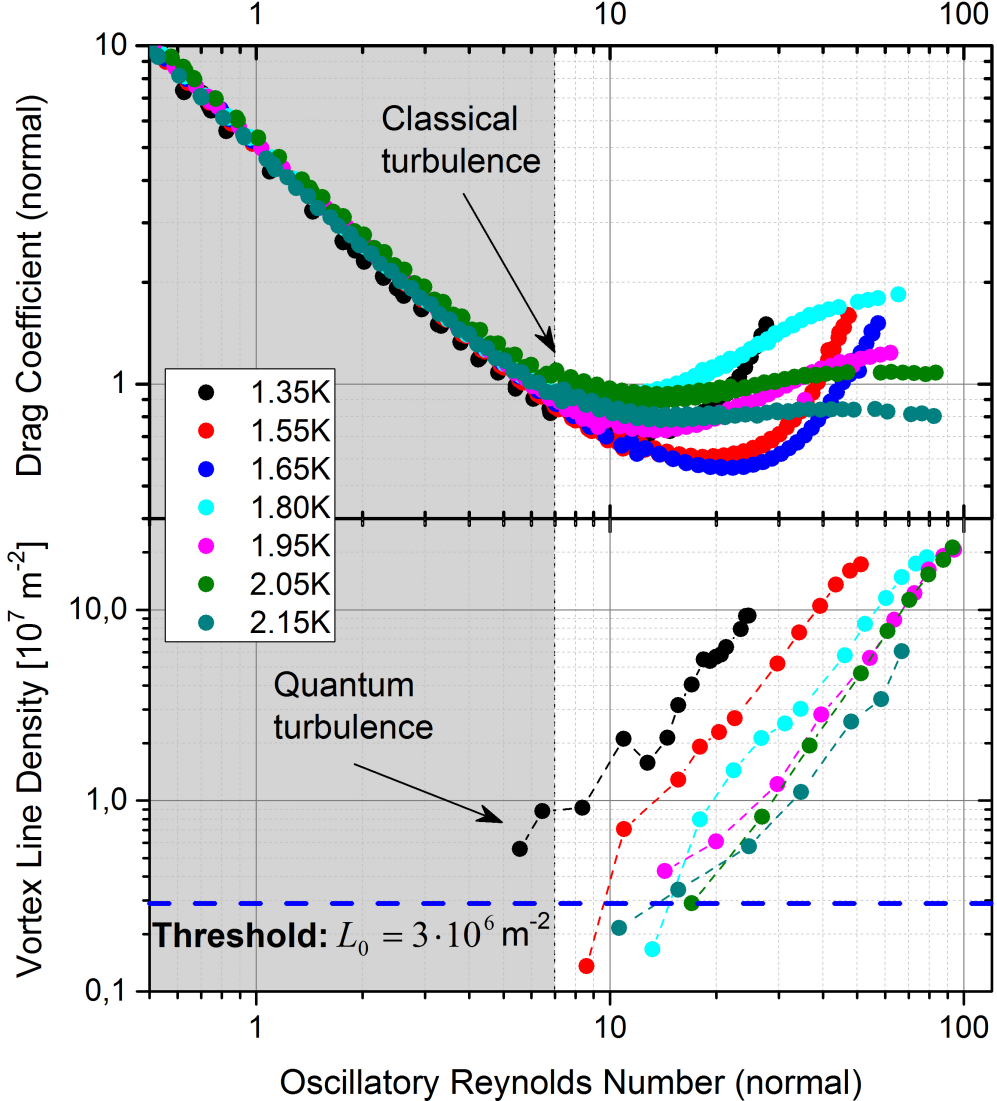


Figure 3.9: Plot of the normal fluid drag coefficient C_{Dn} and vortex line density L against the oscillatory Reynolds number Re_{δ_n} for the fundamental mode of tuning fork.

As shown before, classical turbulence of the normal component arises roughly when exceeding the critical $Re_{\delta_n c} \approx 7$. On the other hand, QT has been detected above $v_c^f \approx 0.3 \text{ m/s}$, so in **Figure 3.9** it is clearly shown that a considerable QT was detected as first only for temperature 1.35 K. However, following the previous set of graphs in **Figure 3.8**, we came to a similar conclusion for all three of the lowest temperatures (1.35 K, 1.55 K, 1.65 K), not just the lowest one. This could be understood in such a manner that although CT could have occurred first for 1.55 K and 1.65 K, QT followed shortly and soon became a dominant contribution to the drag force due to the high density of the superfluid component.

Overtone Mode

Here we perform exactly the same dependencies and similar conclusions we introduced for the fundamental mode in previous **Section 3.3**.

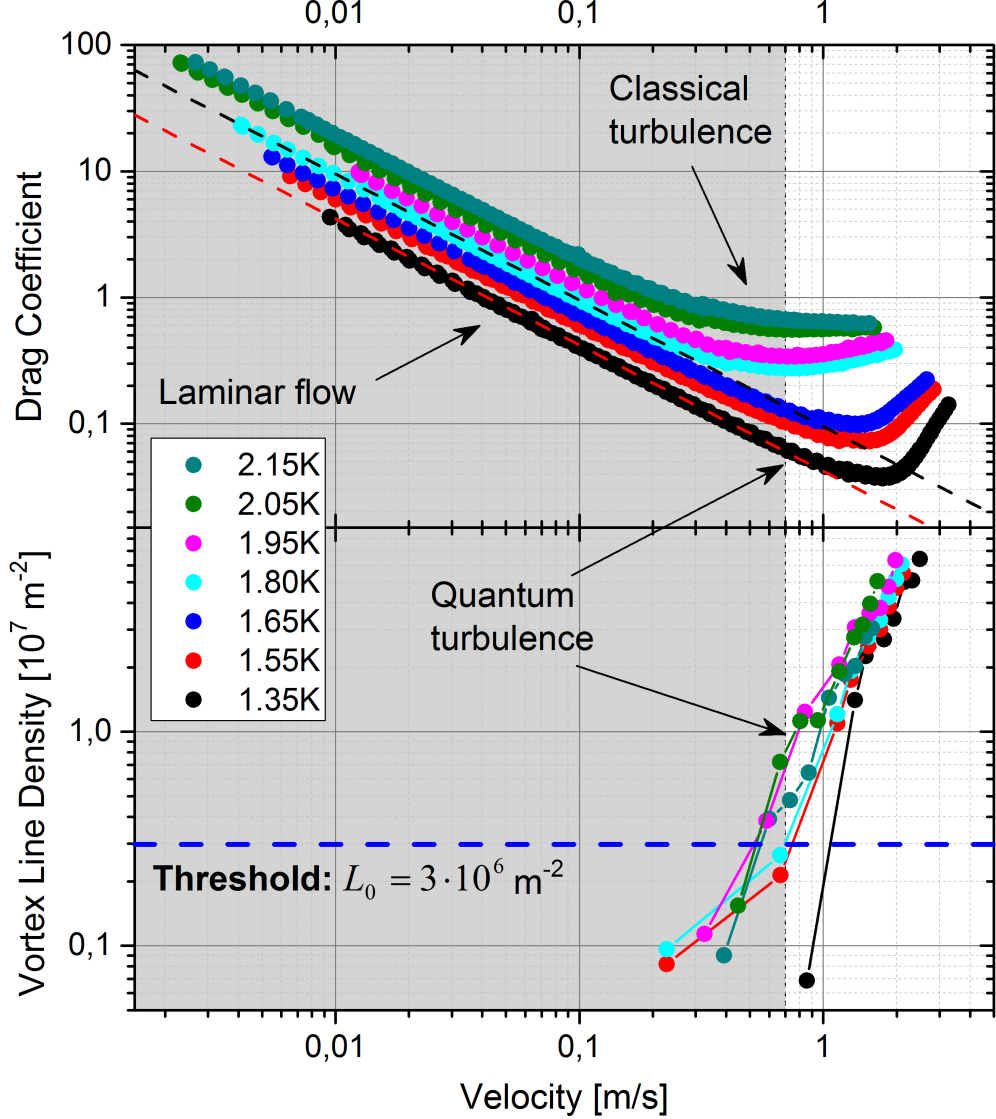


Figure 3.10: Velocity dependence of drag coefficient C_D and vortex line density L for the overtone mode of the tuning fork. The *blue, red and black dotted lines* are the threshold level and laminar drag fits for the 1.35 K and 1.80 K curves, respectively. The *shaded zone* marks sub-critical velocities from the point of view of detection of quantized vortices by second sound, and corresponds to the laminar drag regime for the lowest three temperatures.

The situation for the overtone mode seemingly does not differ from the fundamental - the only difference is that the correlation of QT formation and onset of non-linear drag is harder to see by the naked eye.

The plots of C_{Dn} and L against Re_{δ_n} (shown in **Figure 3.11**) will help to illustrate the order in which the turbulence transitions likely occurred.

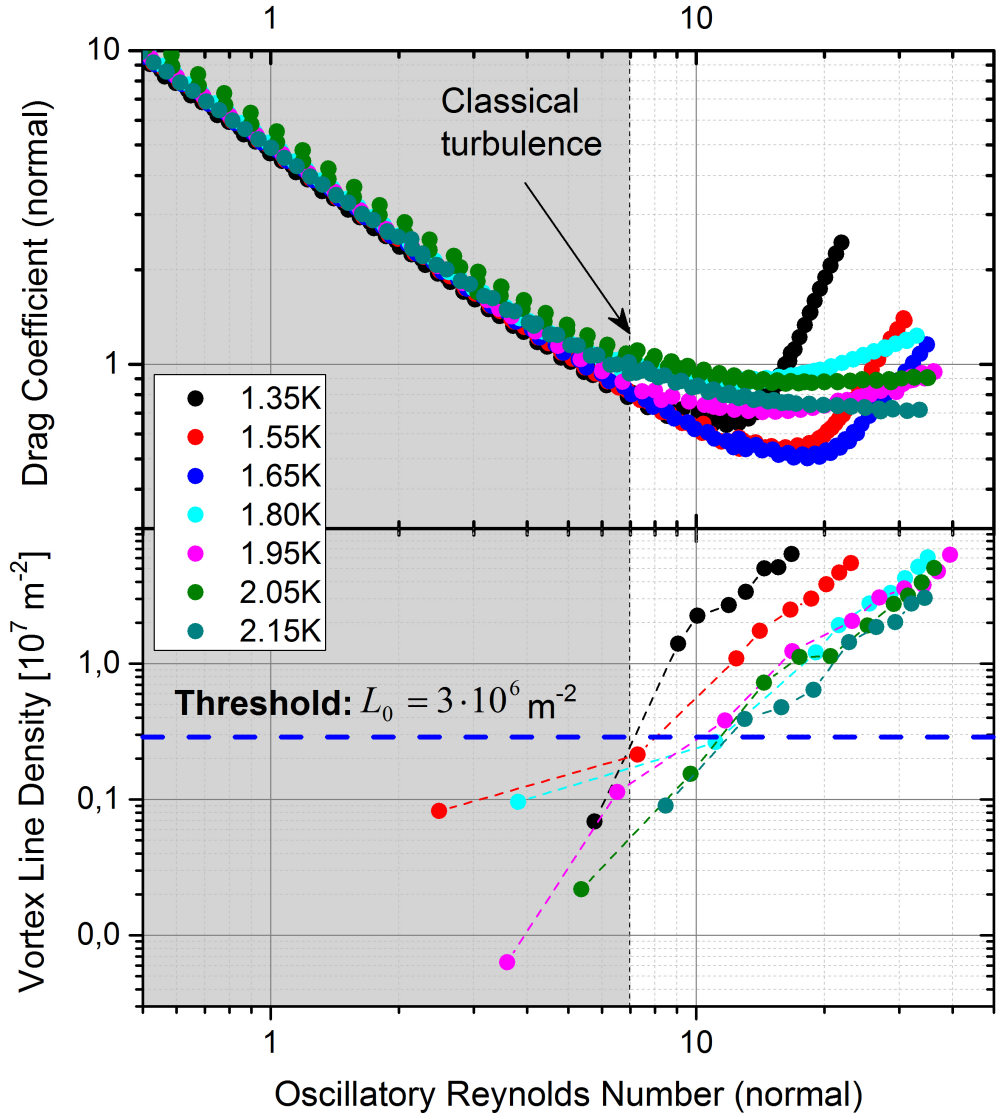


Figure 3.11: Plot of the normal drag coefficient C_{Dn} and vortex line density L against the oscillatory Reynolds number $Re_{\delta n}$ for the overtone mode.

In contrast with the fundamental mode, here measurable QT did not occur earlier than CT at any of the shown temperatures. Although the graph in **Figure 3.10** looked like the displayed non-linearities of the lowest three temperature curves are caused due to the formation of quantized vortices, this does not necessarily have to be true. Similarly to the fundamental mode, CT may have appeared earlier, but QT dominated rapidly and hence CT could not be seen in the drag coefficients reliably.

3.4 Discussion

In this Section we summarize all the observations and found relations between the measured drag forces and the vortex line densities detected by second sound attenuation. We also put together a *flow phase diagram* for better visualisation of the whole concept. To start with, we have already found the following:

- I. Vortex line density measurement** - A significant amount of quantized vortices are produced upon exceeding the temperature-independent critical velocities $\approx 0.3 \text{ m/s}$ and $\approx 0.7 \text{ m/s}$ for the fundamental and overtone modes of the tuning fork, respectively. In addition, the scaling factor for critical velocity generally agrees with the prediction based on quantized vortex dynamics $\sim \sqrt{\kappa\omega}$.
- II. Drag force measurement** - Until a certain oscillatory Reynolds number $\text{Re}_{\delta_{nc}} = 7 \pm 2$ is exceeded, the drag force is linear with velocity. For higher temperatures, where there is considerably less superfluid component, there is a clear transition to a $C_D \approx \text{const.}$ non-linear drag, similar as in classical fluids and likely related to turbulence of the normal component.
- III. Correlations** - The onset of non-linearity for 1.35 K, 1.55 K and 1.65 K curves is definitely caused by the production of quantized vortices, although classical turbulence of normal component appeared earlier in the most of cases, but with negligible effect on drag. In other cases (1.80 K and above), CT dominates as the first.

Flow Phase Diagram

To have a better idea, when each of the turbulences occur, we will attempt to construct a *flow phase diagram*, plotting Re_{δ_n} against velocity and illustrating the areas of non-linear drag forces at each temperature. For the time being, let us consider a much simplified situation where CT and QT do not affect each other, i.e., no interactions between the normal and the superfluid component. Within this first approach, QT is created only when the critical velocity $v_c^f = 0.3 \pm 0.1 \text{ m/s}$ (for fundamental mode) or $v_c^o = 0.7 \pm 0.2 \text{ m/s}$ (for overtone mode) is exceeded and CT forms when exceeding the critical oscillatory Reynolds number $\text{Re}_{\delta_{nc}} = 7 \pm 2$. For a more direct comparison of the two resonant modes of the tuning fork, we additionally rescale the peak velocities by the factor of $\sqrt{\kappa\omega}$, obtaining a *dimensionless velocity*. Whether CT and/or QT occur or not can be then shown using rectangular turbulent zones in a flow phase diagram combining these two quantities.

Let us recall the definition of the oscillatory Reynolds number for normal component:

$$\text{Re}_{\delta_n}(T) = \frac{\rho_n(T)\delta_n(T)v}{\eta(T)} = \sqrt{\frac{2\kappa\eta(T)}{\rho_n(T)}} \cdot \frac{v}{\sqrt{\kappa\omega(T)}}, \quad (3.2)$$

where $\eta(T)$ and $\rho_n(T)$ are temperature dependent viscosity and normal fluid density (experimental values can be found in [19]). According to (3.2), we should get in a log-log flow phase

diagram a set of parallel lines for the different temperatures, intersecting the boundaries of the *turbulent zones* in different order.

Needless to say, this is a gross oversimplification of the real situation, as the presence of any significant amount of quantized vortices will lead to a non-negligible mutual friction force between the two components. At the same time, pressure and velocity fluctuations in any classical turbulence of the normal component may affect the precise moment at which quantized vortices pinned to the surface of the fork start to reconnect and multiply.

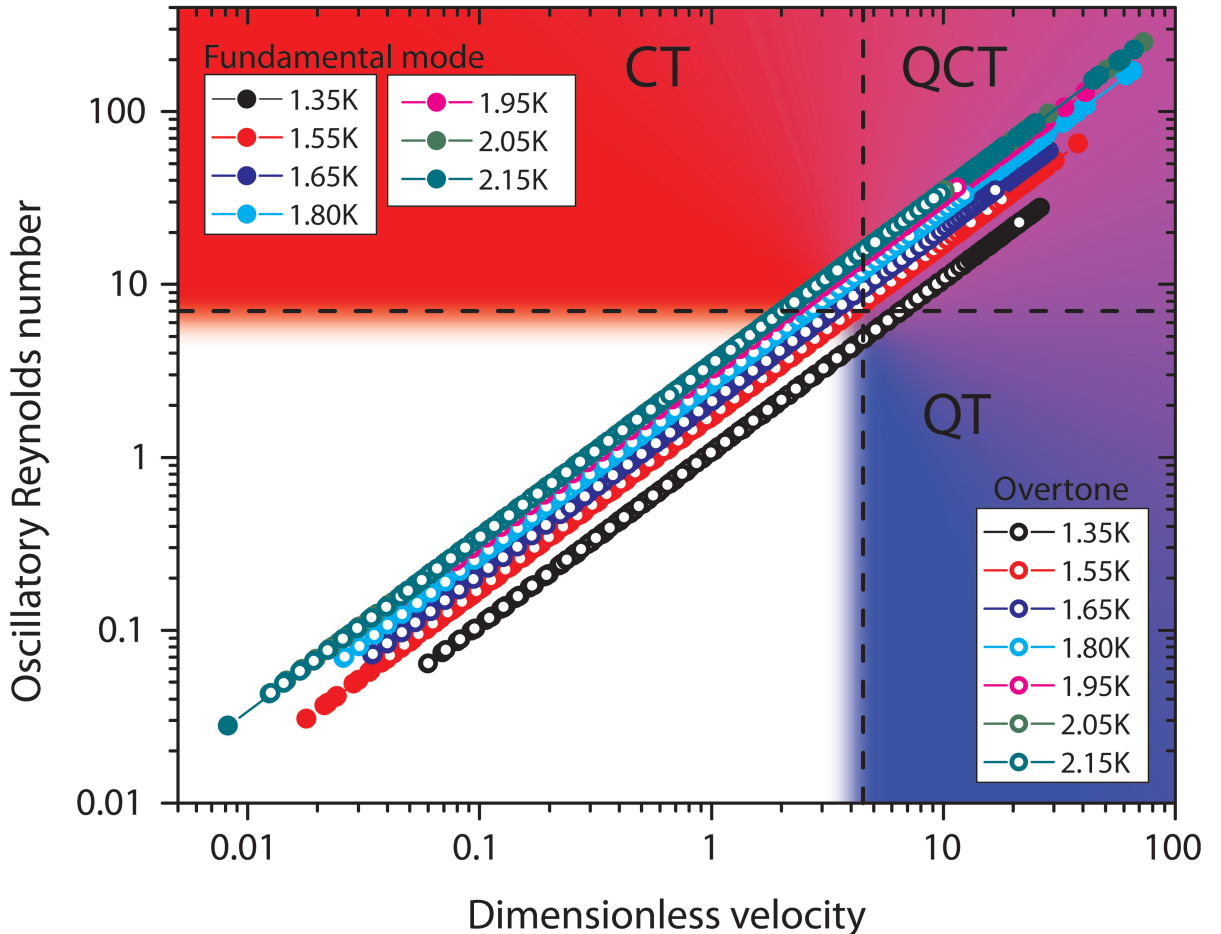


Figure 3.12: The simplified flow phase diagram illustrating the basic conditions for CT and QT to occur in the flow due to the investigated tuning fork. We note that only in the case of 1.35 K curve we are absolutely sure that QT was created first. The vertical and horizontal *black dashed lines* marks the level of critical oscillatory Reynolds number $Re_{\delta_n c} \approx 7$ and dimensionless critical velocity $v_c^f / \sqrt{2\pi\kappa f_0^f} \approx v_c^o / \sqrt{2\pi\kappa f_0^o} \approx 4.5$.

In reality, not only the transitions to CT and/or QT will affect (and possibly help trigger) one another, but one might also suspect that even the intensity of either type of turbulence will bear significant consequences for the other one, due to coupling of the two fluids via the mutual friction force. A more thorough analysis of these effects is clearly required and this topic will be subject of further experimental investigations in an improved realization of the experimental setup.

4. Conclusions

In this Thesis, we have shown data reflecting the tuning fork oscillations in superfluid ^4He bath (at seven different velocities - 1.35 K, 1.55 K, 1.65 K, 1.80 K, 1.95 K, 2.05 K, 2.15 K) as well as the second sound waves propagating through the resonator. The method of second sound attenuation showed that the only relevant parameter related with production of quantized vortices is the velocity amplitude of the fork tip and the (high enough) frequency of oscillation. We estimated the critical velocities for the fundamental and overtone modes to be $v_c^f = 0.3 \pm 0.1 \text{ m/s}$, and $v_c^o = 0.7 \pm 0.2 \text{ m/s}$, respectively, which should scale with the frequency as $\propto \sqrt{\kappa\omega}$. We also confirmed that this scaling is consistent with the obtained critical velocities.

Using results from drag force measurements, a transition from linear to non-linear drag was clearly observed at different velocities for given temperatures. Scaling the force to drag coefficient and the velocity to oscillatory Reynolds number, both with respect to the normal component of ^4He , revealed many hydrodynamic properties of the system. Starting with the fact that only the normal component contributes to the drag force in laminar flow, continuing with dynamical similarity of both fork modes and ending with critical $\text{Re}_{\delta_n c} = 7 \pm 2$, above which the non-linear drag was apparent.

We divided the temperature curves in two categories - those for which the non-linearity seemingly appeared at one certain velocity (strongly correlated with the production of quantized vortices), and those for which the onset arises when exceeding the critical $\text{Re}_{\delta_n c}$. More detailed analysis showed that in the case of fundamental mode, we can safely claim that QT occurred first only for $T = 1.35 \text{ K}$. For the overtone mode, this scenario actually could not be confirmed for any temperature at all. But we have to still keep in mind that due to a relatively high sensitivity threshold and less-than-optimal quality of the second sound signal, it is, at this point, difficult to arrive at more convincing conclusions.

Finally, we introduced the *flow phase diagram* as a good illustrative tool showing each type of turbulence in particular *zones* and each of the temperature curves as a set of parallel lines, intersecting the boundaries of *zones* in different order.

Summary

We summarize all the achieved results and conclusions (denoting "✓" as a positive contribution, "?" as an unresolved question and "✗" as an aspect that should be improved in future) as follows:

- ✓ Fundamental and overtone resonance mode of submerged tuning fork in superfluid ^4He have been found ($f_0^f = 6.38 \text{ kHz}$, $f_0^o = 40.00 \text{ kHz}$).
- ✓ Second sound has been generated and a wide frequency sweep measured. The 1st mode appeared to be the clearest and was used in further measurements.

- ✓ Reliable formation of quantum turbulence above $v_c^f = 0.3 \pm 0.1$ m/s (fundamental) and $v_c^o = 0.7 \pm 0.2$ m/s (overtone) was found to be temperature independent.
- ✓ The theory of critical velocity scaling $v_c \propto \sqrt{\kappa\omega}$ has been found in agreement with the experimental results.
- ✓ We obtained data across 4 orders of magnitude in the dimensionless velocity (from 10^{-2} to 100), which is a remarkably wide range.
- ✓ The oscillatory Reynolds number defined for normal component of superfluid ${}^4\text{He}$ as $\text{Re}_{\delta_n} = \rho_n \delta_n v / \eta$ proved to lead to the correct scaling of the drag forces and turned out to be a useful quantity in our analysis.
- ✓ Onset of non-linear drag has been observed above $\text{Re}_{\delta_{nc}} = 7 \pm 2$ for both fork modes.
- ✓ QT definitely occurs before CT at 1.35 K, while CT occurs first at 2.15 K and 2.05 K. This means that a temperature must exist between these two values, where both types of turbulence are likely to be created at the same time. With the data available, we can estimate this temperature to be close to 1.52 K for the tuning fork used in this study.
- ? Except for the outermost temperatures, we cannot say with certainty which type of turbulence appears first.
- ? The true shape of the *turbulence zones* is still not clear. Without better-resolved measurements, we have only a rough estimate based on the critical velocities and the oscillatory Reynolds number (which may themselves be affected by the sensitivity of the second sound resonator and the unsystematic behaviour of the tuning forks).
- ✗ The sensitivity and quality of second sound sensors should be improved to provide less deviation of critical velocities. This may be achieved, e.g., by using a shorter resonator without a strong connection to the helium bath as the current one had (a 1 mm diameter hole).
- ✗ The unsystematic behaviour of the tuning fork ought to be eliminated. We believe that this is indeed possible, as other experiments with the same tuning fork (even measurements on the dilution fridge in the Prague Laboratory of Superfluidity) have shown no signs of such behaviour. The first steps to be taken is a better isolation of the tuning forks and the entire second sound resonator from the helium bath, such as in a pressure cell or inside an enclosure filled by helium only through superleaks.

This topic (identification of the onset of the different types of turbulence) will definitely need much more experimental (and theoretical) work to clarify what are the conditions to make QT or CT and how these effects can interact.

Bibliography

- [1] KAPITSA, P. *The Super-Fluidity of Liquid Helium II.* Nature **141**, 74 (1938)
- [2] TONG, D. *Statistical physics.* University of Cambridge Part II
- [3] TISZA, L. *The viscosity of liquid helium and the Bose-Einstein statistics.* Comptes Rendus Acad. Sciences, **207**:1186-1189 (1952)
- [4] LANDAU, L.D. and LIFSHITZ, E.M. *Fluid Mechanics,* Second English Edition. Pergamon Books Ltd., (1987). ISBN 0-08-033933-6
- [5] LANDAU, L.D. *The theory of superfluidity of helium II.* J. Phys. USSR, Vol. **11**, 91 (1947)
- [6] ANDRONIKASHVILI, E.L. J. Phys. USSR, **10**, 201 (1946)
- [7] SKRBEK, L. et al. *Fyzika nízkých teplot,* 1. vydání. Praha: MatfyzPress, (2011). ISBN 978-80-7378-168-2.
- [8] VARGA, E. *Second sound as a tool to study He-II flow.* Bachelor thesis (2012).
- [9] OSBORNE, D.V. *The Rotation of Liquid Helium-II.* Proc. Royal Soc. London , **63**: 909-912 (1950)
- [10] FEYNMAN, R.. *Application of quantum mechanics to liquid helium.* Progress in Low Temperature Physics, **1**, 17-53 (1957)
- [11] GUÉNAULT, T. *Basic Superfluids.* Taylor & Francis e-Library (2003). ISBN 0-203-26973-X.
- [12] VINEN, W.F. and HALL, H.E. *The rotation of liquid helium II*
I. *Experiments on the propagation of second sound in uniformly rotating helium II.* Proc. Royal Soc. London **238**:204-214 (1957)
- [13] VINEN, W.F. and HALL, H.E. *The rotation of liquid helium II*
II. *The theory of mutual friction in uniformly rotating helium II.* Proc. Royal Soc. London **238**:215-234 (1957)
- [14] S. BABUIN , M. STAMMEIER, E. VARGA, M. ROTTER, L. SKRBEK *Quantum turbulence of bellows-driven ^4He superflow: Steady state* Phys. Rev. B, **86** (2012)

- [15] VAN DYKE, M. *An Album of Fluid Motion*.
The Parabolic Press, Stanford, California (1982). ISBN 0-915760-02-9
- [16] R. HÄNNINEN, W. SCHOEPE *Dynamical Scaling of the Critical Velocity for the Onset of Turbulence in Oscillatory Superflows*. J. Low Temp. Phys. **164**: 1-4 (2011)
- [17] R. BLAAUWGEERS and col. *Quartz tuning fork: Thermometer, Pressure- and Viscometer for Helium Liquids* Journal of low. temp. phys., Vol. **146**, (2007)
- [18] R.I. BRADLEYS, D. SCHMORANZER and col. *Crossover from hydrodynamic to acoustic drag on quartz tuning forks in normal and superfluid ^4He* . Phys. Rev. B, **85** (2012)
- [19] DONNELLY, R.J., BARENGHI, C.F *The Observed Properties of Liquid Helium at the Saturated Vapor Pressure*. American Ins. of Phys. and Chem. Soc. (1998)
- [20] AHLSTORM, S.L., BRANDLEY, D.I. and col.. *Frequency-dependent drag from quantum turbulence produced by quartz tuning forks in superfluid ^4He* . Phys. Rev. B, **89** (2014)
- [21] BRANDLEY, D.I., GUÉNAULT, A.M. and col. *History Dependence of Turbulence Generated by a Vibrating Wire in Superfluid ^4He at 1.5 K.*
J. Low Temp. Phys. **162**:375-382 (2011)
- [22] VARGA, E., BABUIN, S., SKRBEK, L. *Second-sound studies of coflow and counterflow of superfluid ^4He in channels*. Physics of fluids **27** (2015)
- [23] BRADLEY, D.I., CROOKSTON, P. and col. *Measuring the Prong Velocity of Quartz Tuning Forks Used to Probe Quantum Fluids*. J. Low Temp. Phys. **161**:536-547 (2010)
- [24] BLAŽKOVÁ, M., SCHMORANZER, D. and col. *Generation of turbulence by vibrating forks and other structures in superfluid ^4He* . Phys. Rev. B, **79** (2009)
- [25] JACKSON, M.J. and col. *Measurement of Vortex Line Density Generated by a Quartz Tuning Fork in Superfluid ^4He* . J. Low Temp. Phys. **183**:208-214 (2016)
- [26] BAHYL, J. *Measurement of quantum turbulence in superfluid ^4He* . FMFI ŠVK (2016)